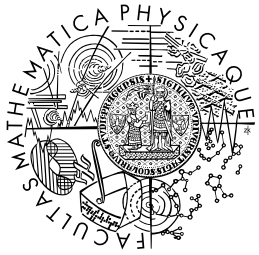

FACULTY
OF MATHEMATICS
AND PHYSICS
Charles University

BACHELOR THESIS

Petr Kos

Optical and magneto-optical spectroscopy of ferimagnetic materials

Institute of Physics of Charles University

Supervisor of the bachelor thesis: RNDr. Martin Veis, Ph.D.
Study programme: Physics
Study branch: Physics

Prague 2024

I declare that I carried out this bachelor thesis independently, and only with the cited sources, literature and other professional sources. It has not been used to obtain another or the same degree.

I understand that my work relates to the rights and obligations under the Act No. 121/2000 Sb., the Copyright Act, as amended, in particular the fact that the Charles University has the right to conclude a license agreement on the use of this work as a school work pursuant to Section 60 subsection 1 of the Copyright Act.

In ..... date ....

Author's signature

A huge thanks goes to my family and friends whose support has been an invaluable gift during my studies. If not for them and their kind words, not only might I have never persuaded myself to study physics, but I would surely not have made it through the challenging initial years. Additionally, I would like to extend my heartfelt gratitude to my supervisor, RNDr. Martin Veis, Ph.D., and my advisor, Mgr. Michal Vančík, whose guidance and mentorship have been indispensable.

Title: Optical and magneto-optical spectroscopy of ferimagnetic materials

Author: Petr Kos

Institute: Institute of Physics of Charles University

Supervisor: RNDr. Martin Veis, Ph.D., Institute of Physics of Charles University

Abstract: This thesis focuses on ferrimagnetic Mn_4N thin films and their gallium-doped versions. Magnetooptical properties of several pure and gallium-doped Mn_4N thin films were examined using spectral magnetooptical Kerr effect (MOKE) measurements and spectroscopic ellipsometry. Spectral dependencies of the diagonal permittivity tensor elements were calculated from ellipsometry results and compared. MOKE rotation and ellipticity spectra were also measured and compared. In the case of pure Mn_4N samples, MOKE spectra were compared with theoretical data from literature to determine which proposed ferrimagnetic structures may be present in the samples. The ferrimagnetic structure FIM_A exhibited the best agreement with experimental data. The possibility of the presence of mixed FIM_A and ncFIM phases was also explored. Temperature-dependent spectral MOKE measurements were used to study compensation temperature. A shift of the compensation temperature from above to below room temperature was observed between doped $Mn_{4-x}Ga_xN$ samples with $x = 0.11$ and $x = 0.20$, agreeing with literature.

Keywords: MOKE Mn_4N spectroscopic ellipsometry compensation temperature

Contents

Introduction

Ferrimagnetic materials usually consist of two antiferromagneticaly coupled sublattices where, unlike in atiferromagnetic materials, the total magnetic moment does not fully cancel out, leaving a non-zero net magnetic moment. Thanks to that, these materials exhibit special properties interesting for industry applications. In the past, ferrimagnetic materials have been used in magneto-optical recording, while more recently, there has been a renewed interest in ferrimagnetic materials for use in high density magnetic random access memories [1].
Mn_4N is a ferrimagnetic material which, unlike most ferrimagnets, does not contain any rare earths elements, making it more attractive for large scale applications. Furthermore, Mn_4N exhibits a large perpendicular magnetic anisotropy and ultrafast response to external field [2], along with other desirable properties [1]. Additionally, magnetic properties of Mn_4N can be modified by doping with other magnetic as well as non-magnetic elements [3].
Magnetic structure of bulk Mn_4N is already known [3], however, there is still much debate about the ferrimagnetic structures present in Mn_4N thin films [2].
In this thesis, optical and magnetooptical methods were used to examine pure and gallium doped Mn_4N thin films. The measurements of pure Mn_4N thin films were compared with theoretical calculations using data from literature [2]. Interestingly enough, we came to a different conclusion than that of the source article [2]. The effect of used substrate on the magnetooptical properties of Mn_4N thin films was also observed and briefly discussed. In case of the gallium doped $Mn_{4-x}Ga_xN$ thin films, we examined three samples with gallium content ranging from $x = 0.11$ to $x = 0.27$. Special attention was given to compensation temperature and its change with the gallium content. We observed a shift of the compensation temperature from above room temperature to bellow room temperature with increasing gallium content in the samples. In the case of one sample, we were able to put a high bound on the possible values of its compensation temperature.

This thesis first introduces electromagnetic waves and a very useful plane wave solution to the wave equation. In the second chapter, polarisation of light is introduced along with Jones calculus, a formalism used to mathematically describe the polarisation of light and its interaction with optical elements. Important magneto-optical observables are also introduced in this chapter. Chapter 3 focuses on the permittivity tensor and how its elements relate to quantities measured by experimental methods used in this thesis. Chapter 4 introduces magnetism and a basic categorisation of magnetic materials with a special attention given to ferrimagnets as they are the focus of this thesis. In chapter 5 experimental techniques used in this thesis are introduced, while chapter 6 summarizes physical properties of Mn4N in pure and Ga doped form. Chapter 7 presents obtained results on measured samples and discusses them within

the context of current literature.

Chapter 1

Electromagnetic waves

Throughout scientific history, it has been shown time and time again, that light is a great probe for studying various material properties. Likewise in this thesis, the experimental methods rely on the interaction of light with the studied sample to provide useful information about its structure and behaviour. To describe the interaction of light with matter (i.e. measured samples), one needs to first describe the light itself. It is a well known fact, that light can be thought of as an oscillating electromagnetic wave. This chapter will focus on the formal derivation of the wave equation from the fundamental Maxwell equations and its special case solution - the plane wave.

1.1 Wave equation

The Maxwell equations are a set of coupled partial differential equations that form the fundamental building blocks of all of classical electromagnetism and optics. These equations link the electric field intensity $\mathbf{E}$, magnetic induction $\mathbf{B}$, magnetic field $\mathbf{H}$, free charge density ρ and free current density $\mathbf{j}$ [4]

$$\nabla \times \mathbf{E} + \frac{\partial \mathbf{B}}{\partial t} = 0\,, \tag{1.1}$$

$$\nabla \cdot \mathbf{B} = 0\,, \tag{1.2}$$

$$\nabla \times \mathbf{H} - \frac{\partial \mathbf{D}}{\partial t} = \mathbf{j}\,, \tag{1.3}$$

$$\nabla \cdot \mathbf{D} = \rho\,. \tag{1.4}$$

To derive the electromagnetic wave equation the constitutive relations

$$\mathbf{D} = \varepsilon_0 \boldsymbol{\varepsilon} \mathbf{E}\,, \tag{1.5}$$

$$\mathbf{B} = \mu_0 \boldsymbol{\mu} \mathbf{H}\,, \tag{1.6}$$

linking $\mathbf{E}$ and $\mathbf{B}$ with $\mathbf{D}$ and $\mathbf{H}$ along with the Ohms law

$$\mathbf{j} = \boldsymbol{\sigma} \mathbf{E}\,, \tag{1.7}$$

are assumed to hold true. Standard notation is used here, where $\boldsymbol{\varepsilon}$ is the relative permittivity tensor, ε_0 is the permittivity of vacuum, $\boldsymbol{\mu}$ is the relative permeability

tensor, μ_0 is the permeability of vacuum and $\boldsymbol{\sigma}$ is the conductivity tensor. Relationships 1.5, 1.6 and 1.7 disregard any non-linear effects as they are negligible for weak fields. Furthermore a static medium is assumed, making $\boldsymbol{\varepsilon}$, $\boldsymbol{\mu}$ and $\boldsymbol{\sigma}$ time-independent. For most light-matter interactions, the magnetic field component is very weak compared to the electric field component and can thus be neglected ($\boldsymbol{\mu} \approx 1$). Substituting 1.6 into 1.2 and 1.5 along with substituting 1.7 into 1.3 we get

$$\frac{1}{\mu_0}\nabla \times \mathbf{E} + \frac{\partial \mathbf{H}}{\partial t} = 0\,, \tag{1.8}$$

$$\nabla \mathbf{H} - \boldsymbol{\varepsilon}\varepsilon_0 \frac{\partial \mathbf{E}}{\partial t} - \boldsymbol{\sigma}\mathbf{E} = 0\,. \tag{1.9}$$

Taking the curl of 1.8, the partial derivative of 1.9, combining the two equations and using the vector identity

$$\nabla \times (\nabla \times \mathbf{A}) = \nabla(\nabla \cdot \mathbf{A}) - \Delta \mathbf{A}$$

valid for an arbitrary vector $\mathbf{A}$, yields the electromagnetic wave equation

$$\Delta \mathbf{E} - \varepsilon_0 \mu_0 \boldsymbol{\varepsilon} \frac{\partial^2 \mathbf{E}}{\partial t^2} - \mu \boldsymbol{\sigma} \frac{\partial \mathbf{E}}{\partial t} - \nabla(\nabla \cdot \mathbf{E}) = 0\,. \tag{1.10}$$

1.2 Electromagnetic waves in a vacuum

For an electromagnetic wave travelling through a vacuum, we have $\boldsymbol{\sigma} = 0$ and $\rho = 0$ as there can be no free currents or charges. From equations 1.4 and 1.5 we see that $\rho = 0$ leads to the condition $\nabla \cdot \mathbf{E} = 0$. Also, for a vacuum it holds true that $\boldsymbol{\varepsilon} = 1$. Thus equation 1.10 simplifies to

$$\Delta \mathbf{E} - \mu_0 \varepsilon_0 \frac{\partial^2 \mathbf{E}}{\partial t^2} = 0\,. \tag{1.11}$$

Equation 1.11 has a simple and elegant solution in the form of a monochromatic, time-harmonic plane wave

$$\mathbf{E}(\mathbf{r}, t) = \mathbf{E_0} \cos\left(\omega t - \mathbf{k} \cdot \mathbf{r} + \delta\right) = \mathrm{Re}\Big\{\mathbf{E_0} e^{i(\omega t - \mathbf{k}\cdot\mathbf{r} + \delta)}\Big\}\,, \tag{1.12}$$

where $\mathbf{r}$, $\mathbf{E_0}$, $\mathbf{k}$ and δ stand for the position vector, wave amplitude, wave vector and initial phase respectively. Furthermore, comparing relation 1.11 with the general wave equation, we can also write down a relationship for the speed of light in a vacuum $c = 1/\sqrt{\mu_0 \varepsilon_0}$. The plane wave solution is widely used for a large variety of problems in optics. For the next chapter, it will be important to note that for a plane wave, $\mathbf{k}$, $\mathbf{E}$ and $\mathbf{B}$ are all perpendicular to each other, which can be easily derived by plugging the plane wave solutions for $\mathbf{B}$ and $\mathbf{E}$ back into the Maxwell equations. Although the plane wave solution was derived here for vacuum conditions, it is assumed to be a valid solution for a significantly wider range of problems. In the next chapter of this thesis, solution 1.12 will be used to describe the polarisation of light.

Chapter 2

polarisation of light

The previous chapter showed, that light is an electromagnetic wave. Furthermore, in most cases it is sufficient to think only about the electric field vector. It was then shown that for special conditions, the light wave is a plane wave with planar wavefronts perpendicular to the direction of travel. This chapter will take a look at how the way the electric field vector oscillates in a given plane influences its interaction with matter and how one can describe this behavior for a special case of totally polarised light. Furthermore we will take a look at how an external magnetic field can influence this interaction and derive an equation for the so called *Kerr rotation* fundamental for this thesis.

2.1 What is polarisation

As described in the previous chapter, electromagnetic wave travelling through a vacuum has the form of a plane wave 1.12. Assuming that the wave is travelling in the z direction, the components of the electric field vector can without the loss of generality be written as

$$E_x(z,t) = E_{0x}\cos\left(\omega t - kz + \delta_x\right), \tag{2.1}$$

$$E_y(z,t) = E_{0y}\cos\left(\omega t - kz + \delta_y\right), \tag{2.2}$$

$$E_z = 0\,, \tag{2.3}$$

where $E_x(z,t)$, $E_y(z,t)$ and δ_x, δ_y are amplitudes and phase offsets of the corresponding field components respectively. We can therefore see that the electric field oscillations can be represented as a linear combination of two plane waves with the same frequency, where one of them is oscillating only along the x axis and the other one only along the y axis. The relationship between $E_x(z,t)$ and $E_y(z,t)$ describes the polarisation of light. In general, the electric field vector traces an ellipse in a plane perpendicular to the wave vector at a given point [5]. We call the traced ellipse the ellipse of polarisation. Lets note here that there are two often used special cases of polarisation. When the electric field vector traces a line instead of the ellipse we talk about *linearly polarised light* and when it traces a circle, we talk about *circularly polarised light*. The ellipse of polarisation is determined by four parameters. These parameters are defined when looking at the ellipse *against* the direction of the wave vector $\mathbf{k}$. They are as follows:

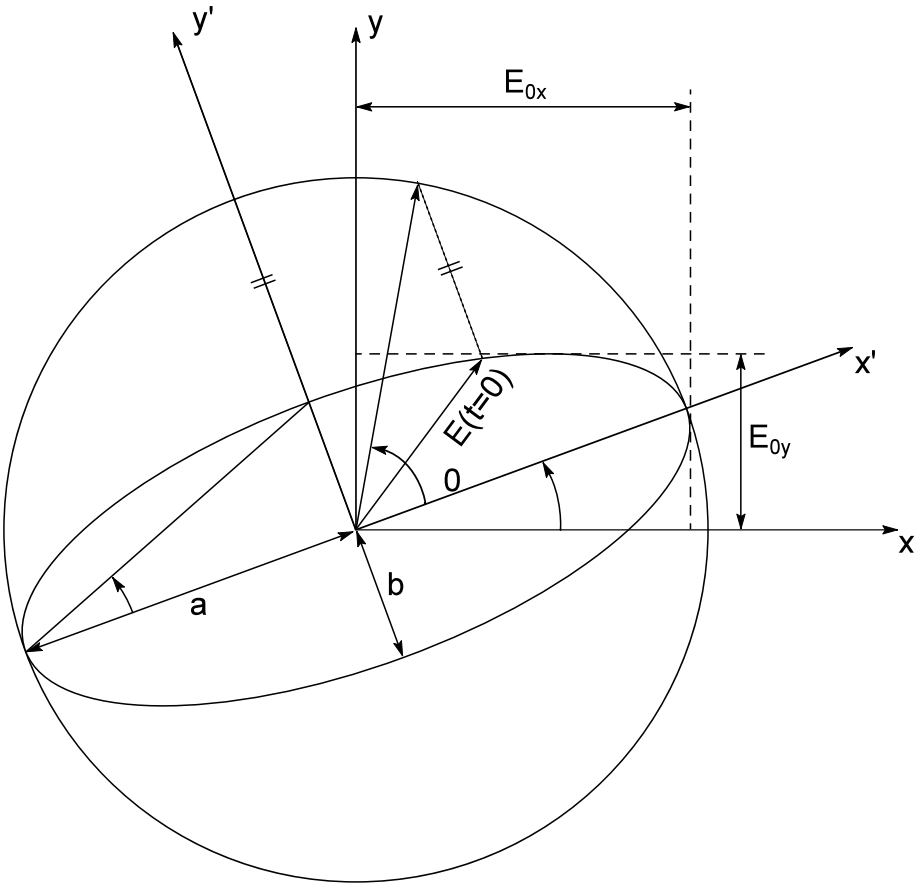

Figure 2.1: Polarisation ellipse

- The azimuth θ - an oriented angle between the x axis and the major axis of the ellipse. It can take values from $-\pi/2$ to $\pi/2$. Its values are positive, when the orientation is counter-clockwise
- The ellipticity e - defined as $e = b/a$, where b and a are lengths of the semi-major and semi-minor ellipse axis respectively. It is also useful to define the ellipticity angle ϵ satisfying the relationship $e = \tan\epsilon$. Its values range from $-\pi/4$ to $\pi/4$. In this thesis, the ellipticity will be positive, when the ellipse is traced in the clockwise sense (right handed polarisation) and negative, when the ellipse is traced in the counter-clockwise sense (left handed polarisation).
- The amplitude E_{00} - defined simply as $E_{00} = \sqrt{a^2 + b^2}$ is related to the overall wave intensity $I \approx E_{00}^2$.
- The absolute phase δ_0 - an oriented angle between the electric field vector E at $t = 0$ and the major axis of the ellipse. Here this angle is measured on the projection of $E(t = 0)$ to a circle with the diameter equal to the semi-major axis of the ellipse [6].

Often when one is not interested in studying any interference phenomena, only the azimuth and ellipticity are needed to describe the polarisation state.
It is important to note here, that in general, light can also be partially polarised or completely unpolarised. This can happen in the case of polychromatic light and won't be explored further in this thesis.

2.2 Describing polarised light

When describing polarised light and its transformation by optical elements, one can use 4-component Stokes vectors and corresponding Muller matrices. However, when dealing only with totally polarised light, it is more sensible to use Jones formalism which offers a simpler description albeit at the cost of not being able to deal with depolarisation and partially polarised light. In laboratory environment, the polarisation state of light is usually easily controlled and thus Jones formalism is sufficient.

2.2.1 Jones vectors

The main building block of Jones calculus is the Jones vector - a vector from two-dimensional complex vectorial space elegantly describing the polarisation of light. Rewriting 2.1 and 2.2 as components of a two dimensional vector and introducing a complex amplitude $A_i = E_{0i}e^{i\delta_i}$ we get

$$\mathbf{E}(z,t) = \begin{bmatrix} E_{0x}\cos\left(\omega t - kz + \delta_x\right) \\ E_{0y}\cos\left(\omega t - kz + \delta_y\right) \end{bmatrix} = \begin{bmatrix} \mathrm{Re}\left\{A_x e^{i(\omega t - kz)}\right\} \\ \mathrm{Re}\left\{A_y e^{i(\omega t - kz)}\right\} \end{bmatrix} . \tag{2.4}$$

The term $e^{i(\omega t - kz)}$ is same for both components and can therefore be omitted for the discussion of polarisation. The Jones vector is than defined as

$$\mathbf{J} = \begin{bmatrix} E_{0x}e^{i\delta_x} \\ E_{0y}e^{i\delta_y} \end{bmatrix} = \begin{bmatrix} A_x \\ A_y \end{bmatrix} \tag{2.5}$$

Since the absolute value of intensity is often not important, the Jones vector is usually normalised. If we now define a parameter α and phase difference δ

$$\tan\alpha = E_{0y}/E_{0x}\,, \tag{2.6}$$

$$\delta = \delta_y - \delta_x\,, \tag{2.7}$$

we can rewrite relation 2.5 as

$$\mathbf{J} = \begin{bmatrix} \cos\alpha \\ \sin\alpha\, e^{i\delta} \end{bmatrix} . \tag{2.8}$$

Because Jones vectors are vectors, they have to be expressed with regards to some basis. In the previous text we have been working with the Cartesian basis of linear polarisation as it is perhaps the most intuitive approach. In general, however, Jones vectors can be defined for an arbitrary basis consisting of two independent polarisations. In practise there are two widely used polarisation basis of special importance:

- The Cartesian basis

$$\mathbf{J_x} = \begin{bmatrix} 1 \\ 0 \end{bmatrix} , \mathbf{J_y} = \begin{bmatrix} 0 \\ 1 \end{bmatrix} . \tag{2.9}$$

- And the circular basis

$$\mathbf{J_{LCP}} = \frac{1}{\sqrt{2}}\begin{bmatrix} 1 \\ -i \end{bmatrix} , \mathbf{J_{RCP}} = \frac{1}{\sqrt{2}}\begin{bmatrix} 1 \\ i \end{bmatrix} , \tag{2.10}$$

  where indices LCP and RCP denote left handed and right handed circular polarisation respectively.

The Cartesian representation is useful because it provides a simple geometric interpretation of the polarisation state, the circular representation is useful for systems where the circular polarisations can propagate independently.

It will be important later, to be able to transform vectors and matrices into a new basis rotated by an angle φ. Vector rotation is accomplished by using a rotation matrix $\mathbf{R}(\varphi)$ defined as

$$\mathbf{R}(\varphi) = \begin{bmatrix} \cos\varphi & -\sin\varphi \\ \sin\varphi & \cos\varphi \end{bmatrix} . \tag{2.11}$$

It than follows from linear algebra, that

$$v' = \mathbf{R}(\varphi)v , \tag{2.12}$$

$$\mathbf{Q}' = \mathbf{R}(\varphi)\mathbf{Q}\mathbf{R}^{-1}(\varphi) , \tag{2.13}$$

where v is a vector, $\mathbf{Q}$ is matrix and v' and $\mathbf{Q}'$ is the same vector and matrix described in the rotated basis.

2.2.2 Jones matrices

It has been estabilished, that light polarisation can be represented using Jones vectors, but we still need a representation for various optical elements and their interaction with polarised light. Here, Jones matrices are an ideal tool. Suppose we have a light wave heading towards an optical element. We describe the polarisation state of such light wave with a Jones vector using a coordinate system $\mathbf{S}^{(I)}$, where the z axis coincides with the wave vector. When impacting an optical element, part of the wave reflects and a part is transmitted through the element as shown in figure 2.2.

Since in both cases the wave vector changed its direction in the interaction, we need a new coordinate system $\mathbf{S}^{(R)}$ to describe the reflected wave and another system $\mathbf{S}^{(T)}$ to describe the transmitted wave so that the z axes again coincide with the wave vectors. To study how the polarisation changes in the interaction, it first needs to be decided in which basis one wants to describe the Jones vectors. The most common choice is a linear basis with one basis vector perpendicular and one parallel to the plane of incidence. The corresponding polarisations are called s-polarisation and p-polarisation respectively.

Now all that needs to be done is to find a matrix, such that when multiplied by the initial Jones vector, we get a Jones vector describing the light polarisation after the interaction. For example, for the reflected wave described by Jones vector $\mathbf{J}^{(R)}$ and incident wave described by the Jones vector $\mathbf{J}^{(I)}$, we need to find a Jones reflection matrix $\mathbf{R}_{sp}$, such that

$$\mathbf{J}^{(R)} = \mathbf{R}_{sp}\mathbf{J}^{(I)} . \tag{2.14}$$

Using the definition 2.5 for the Jones vector along with the aforementioned s, p-polarisation basis, relationship 2.20 can be rewritten in terms of individual elements as

$$\begin{bmatrix} A_s^{(R)} \\ A_p^{(R)} \end{bmatrix} = \begin{bmatrix} r_{ss} & r_{sp} \\ r_{ps} & r_{pp} \end{bmatrix} = \begin{bmatrix} A_s^{(I)} \\ A_p^{(I)} \end{bmatrix} , \tag{2.15}$$

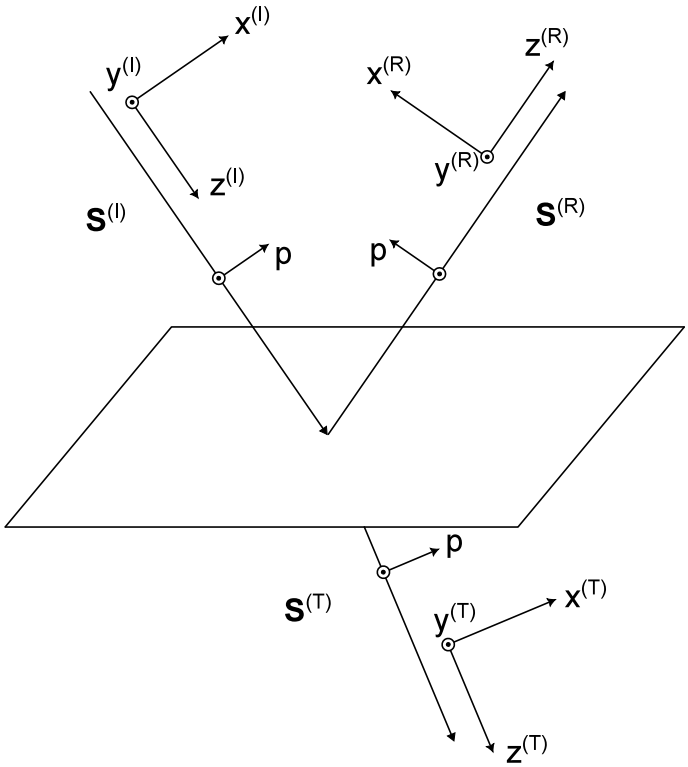

Figure 2.2: Interaction of light with an optical element

where the matrix elements satisfy

$$r_{ss} = \left(\frac{A_s^{(R)}}{A_s^{(I)}} \right)_{A_p^{(I)}=0} , \tag{2.16}$$

$$r_{sp} = \left(\frac{A_s^{(R)}}{A_p^{(I)}} \right)_{A_s^{(I)}=0} , \tag{2.17}$$

$$r_{ps} = \left(\frac{A_p^{(R)}}{A_s^{(I)}} \right)_{A_p^{(I)}=0} , \tag{2.18}$$

$$r_{pp} = \left(\frac{A_p^{(R)}}{A_p^{(I)}} \right)_{A_s^{(I)}=0} . \tag{2.19}$$

Similarly, for the trasmitted wave, we are looking for a transmission Jones matrix $\mathbf{T}_{sp}$ such that

$$\mathbf{J}^{(T)} = \mathbf{T}_{sp}\mathbf{J}^{(I)} , \tag{2.20}$$

or in terms of the individual elements with the help of relationship 2.5 and s, p-polarisation basis

$$\begin{bmatrix} A_s^{(T)} \\ A_p^{(T)} \end{bmatrix} = \begin{bmatrix} t_{ss} & t_{sp} \\ t_{ps} & t_{pp} \end{bmatrix} = \begin{bmatrix} A_s^{(I)} \\ A_p^{(I)} \end{bmatrix} , \tag{2.21}$$

where these elements again satisfy

$$t_{ss} = \left(\frac{A_s^{(T)}}{A_s^{(I)}} \right)_{A_p^{(I)}=0} , \tag{2.22}$$

$$t_{sp} = \left(\frac{A_s^{(T)}}{A_p^{(I)}} \right)_{A_s^{(I)}=0} , \tag{2.23}$$

$$t_{ps} = \left(\frac{A_p^{(T)}}{A_s^{(I)}} \right)_{A_p^{(I)}=0} , \tag{2.24}$$

$$t_{pp} = \left(\frac{A_p^{(T)}}{A_p^{(I)}} \right)_{A_s^{(I)}=0} . \tag{2.25}$$

In case of an optically isotropic sample, the matrices $\mathbf{T}_{sp}$ and $\mathbf{R}_{sp}$ are diagonal, indicating no interaction between the s and p polarisations. The diagonal elements of $\mathbf{T}_{sp}$ and $\mathbf{R}_{sp}$ are related to the sample structure and its optical properties. When the sample is optically anisotropic, the off-diagonal elements of $\mathbf{T}_{sp}$ and $\mathbf{R}_{sp}$ become in general non-zero [6].
Jones matrices can be used to describe changes in polarisation states due to interactions with various optical elements. If light propagates through multiple optical elements one can find the Jones matrix $\mathbf{X}_F$ describing the cumulative effect of all the optical elements simply by multiplying Jones matrices of the individual optical elements $\mathbf{X}_1$, $\mathbf{X}_2$,..., $\mathbf{X}_N$, together

$$\mathbf{X}_F = \mathbf{X}_N \mathbf{X}_{N-1} ... \mathbf{X}_1 . \tag{2.26}$$

Indices in equation 2.26 follow the order in which light interacts with the various optical elements.
We will make use of this formalism in the following chapters when deriving the effects of an experimental apparatus along with the sample on the light polarisation state.

2.2.3 Complex polarisation parameter

In the previous sections we have established that the polarisation state can be described using just two parameters, either the azimuth ϕ and ellipticity angle ϵ, or phase difference δ and the parameter α that were introduced in the relations 2.6 and 2.7. These two sets of parameters are related by equations [5]

$$\tan 2\phi = \tan 2\alpha \cos \delta , \tag{2.27}$$

$$\sin 2\epsilon = \sin 2\alpha \sin \delta . \tag{2.28}$$

However, Jones vector has two complex components and so in general it can contain information not only about the polarisation state itself, but also about the amplitude and the absolute phase. As already mentioned, one is usually not interested in the amplitude, and so the Jones vectors are often normalised. This leaves us with three available parameters, one of them being the absolute phase of the wave. If the total phase is not needed, we can divide the Jones vector by its first component. The resulting Jones vector will have the first component equal to one. The second component will be a complex number containing the whole information about the polarisation state. We call this number χ the *complex polarisation parameter*. If we follow the aforementioned

procedure, we get a definition for χ in the form of

$$\chi = \frac{A_y}{A_x} = \tan(\alpha) e^{i\delta} . \tag{2.29}$$

Suppose now, that we have a polarisation ellipse with azimuth $\phi = 0$ and ellipticity angle ϵ. Than from 2.27 and 2.28 it follows that $\delta = \pi/2$ and $\alpha = \epsilon$. From there, we can construct Jones vector $\mathbf{J}_{0,\epsilon}$ using 2.8 and rotate it by the azimuth ϕ to get

$$\mathbf{J}_{\phi,\epsilon} = \mathbf{R}(\phi)\mathbf{J}_{\epsilon,0} = \begin{bmatrix} \cos\phi & -\sin\phi \\ \sin\phi & \cos\phi \end{bmatrix} \begin{bmatrix} \cos\epsilon \\ i\sin\epsilon \end{bmatrix} = \begin{bmatrix} \cos\epsilon\cos\phi - i\sin\epsilon\sin\phi \\ \cos\epsilon\sin\phi + i\sin\epsilon\cos\phi \end{bmatrix} . \tag{2.30}$$

Using 2.5 and substituting 2.30 into 2.29 we get

$$\chi = \frac{\sin\phi\cos\epsilon + i\cos\phi\sin\epsilon}{\cos\phi\cos\epsilon - i\sin\phi\sin\epsilon} = \frac{\tan\phi + i\tan\epsilon}{1 - i\tan\phi\tan\epsilon} . \tag{2.31}$$

If we now assume small angles ϕ and ϵ, make use of the small angle approximation $\tan x \approx x$ and neglect the second order term in the denominator, we get

$$\chi \approx \phi + i\epsilon . \tag{2.32}$$

It should be emphasised, that relation 2.32 was obtained with respect to the *Cartesian basis of linear polarisations*.

2.3 Magnetooptical observables

The term magnetooptical observables refers to a set of parameters describing changes in the polarisation state of light interacting with a magnetized sample in an external magnetic field. This thesis will be concerned about two particular magnetooptical observables - the Kerr rotation and the Kerr ellipticity. These parameters describe the change in the light polarisation state induced after a reflection on the magnetised sample known as the magnetooptical Kerr effect (MOKE). There is an analogous set of parameters - the Faraday rotation and ellipticity, describing polarisation state changes upon a transmission through the sample.
Before continuing further, lets briefly discuss the main geometrical configurations of the magnetisation vector $\mathbf{M}$ relative to the sample surface and the plane of incidence used in MOKE experiments. There are three main geometrical configurations: polar geometry, longitudinal geometry and transverse geometry. In *polar geometry*, the magnetisation vector is perpendicular to the sample surface. In the *longitudinal geometry*, the magnetisation vector points along the the sample surface and is parallel with the plane of incidence. In the *transverse geometry*, the magnetisation vector also points along sample surface, but is now perpendicular to the plane of incidence. The situation for these three geometries is illustrated in figure 2.3.

For different geometrical configurations, there are different criteria for the Jones matrices describing the change of the polarisation state brought by the reflection on the sample. The criteria stem from symmetry arguments brought by the symmetry of the problem (i.e. the geometrical configuration). For the polar configuration with light travelling perpendicular to the sample surface, which if of main interest for this

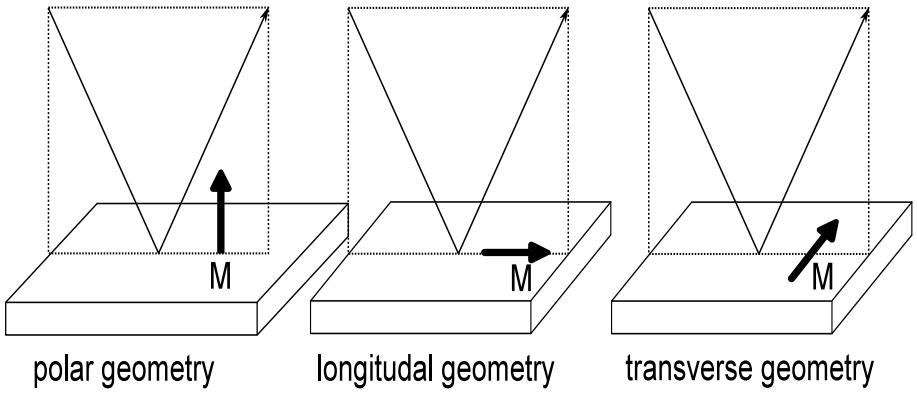

Figure 2.3: Definitions of polar, longitudinal and transverse geometries for MOKE measurements

thesis, the Jones matrix should be invariant with respect to any rotation of angle α about the z axis. In matrix form, this means

$$\mathbf{R_{sp}} = \mathbf{R}(\alpha)\mathbf{R_{sp}}\mathbf{R}(\alpha)\,, \tag{2.33}$$

where we use notation introduced in the previous sections. Equation 2.33 provides an important relationship for the two diagonal and the two offdiagonal elements of the reflection Jones matrix $\mathbf{R}_{sp}$

$$r_{ps} = r_{sp}\,, \tag{2.34}$$

$$r_{ss} = -r_{pp} \tag{2.35}$$

However, for light traveling perpendicular to the sample surface, there is no physical difference between s and p polarisations, therefore, we expect any quantity to be equal for both s and p polarisations.
Lets now get back to the magnetooptical observables. Consider an s-polarised wave reflecting on a magnetised material. As discussed before, for a magnetised material, the off diagonal elements of the Jones reflection matrix $\mathbf{R}_{sp}$ will in general be non zero. We can use 2.16 and 2.17 to express the ratio of the off-diagonal to the diagonal elements of the reflection matrix for an incident s-polarised wave

$$\frac{r_{ps}}{r_{ss}} = \left(\frac{A_p^{(R)}}{A_s^{(R)}}\right)_{A_p^{(I)}=0} = \chi_s^{(R)}\,. \tag{2.36}$$

Which can be further simplified assuming small angles θ_s ϵ_s analogously to 2.31. Using this, we get

$$\chi_s^{(R)} \approx \theta_s^{(R)} + i\epsilon_s^{(R)}\,. \tag{2.37}$$

Let‘s now define the complex magneto-optical Kerr angle $\phi_{K,s}$ and the real Kerr rotation $\theta_{K,s}$ along with the Kerr ellipticity $\epsilon_{K,s}$ for an s-polarised wave as

$$\phi_{K,s} := -\frac{r_{ps}}{r_{ss}} = -\chi_s^{(R)}\,, \tag{2.38}$$

$$\phi_{K,s} \approx \theta_{K,s} - i\epsilon_{K,s} \tag{2.39}$$

Comparing 2.38 and 2.39 with 2.37 the following relations can easily be deduced

$$\theta_{K,s} = -\theta_s^{(R)}\,, \tag{2.40}$$

$$\epsilon_{K,s} = \epsilon_s^{(R)}\,. \tag{2.41}$$

For a p-polarised wave, the complex magneto-optical Kerr angle $\phi_{K,p}$, the real Kerr rotation $\theta_{K,p}$ and the Kerr ellipticity $\epsilon_{K,p}$ are defined analogously as

$$\phi_{K,p} = \frac{r_{sp}}{r_{pp}} \,, \tag{2.42}$$

$$\phi_{K,p} \approx \theta_{K,p} - i\epsilon_{K,p} \,, \tag{2.43}$$

where the second relationship again only holds for small angles $\theta_{K,p}$ and $\epsilon_{K,sp}$.

As discussed before in this section, for polar geometry with light propagating perpendicularly to the sample surface, the relations 2.34 and 2.35 must hold. At the the same time, since s and p polarisation cannot be clearly defined for normal incidence, we expect any physical quantity, to be the same for both aforementioned polarisations. This explains the opposite choice of signs in definitions 2.38 and 2.42.

Chapter 3

Electromagnetic waves in anisotropic media

This chapter looks in more detail at the permittivity tensor first introduced in chapter 1. We discuss the effect of symmetry on its general form, mainly in case of the polar geometry, and briefly introduce the Lorentz and Drude dispersion models. After that, this chapter describes electromagnetic waves propagating through an anisotropic medium and derives important equations linking the off diagonal elements of the permittivity tensor with the Kerr rotation angle and ellipticity derived in chapter 2.

3.1 Permittivity tensor

When using the electromagnetic theory of Maxwell, one describes the magnetooptical effects in terms of the permittivity tensor of a given material. In this thesis, the permittivity tensor was first mentioned in chapter 1, where it was used while deriving the electromagnetic wave equation 1.10. Knowing the permittivity tensor of a material constitutes a very powerful information, that can be used for a wide variety of calculations and can hint at possible real-world applications. Its spectral dependence also carries an important information about inner electronic structure of the material. Furthermore, we can use it to calculate the reflection coefficients and in turn, the Kerr angle. Importantly for special circumstances, this can be reversed and the permittivity tensor can be computed from a measured Kerr angle.

In general, the permittivity tensor in a second-order tensor denoted as

$$\boldsymbol{\varepsilon} = \begin{bmatrix} \varepsilon_{xx} & \varepsilon_{xy} & \varepsilon_{xz} \\ \varepsilon_{yx} & \varepsilon_{yy} & \varepsilon_{yz} \\ \varepsilon_{zx} & \varepsilon_{zy} & \varepsilon_{zz} \end{bmatrix} . \tag{3.1}$$

3.1.1 Symmetry arguments

Lets first deduce a general form of the permittivity tensor for an isotropic magnetic material inserted into a magnetic field. The field can be thought of as a small perturbation of the system. The permittivity tensor can, in the Cartesian representation, be therefore expressed as [7]

$$\varepsilon_{ij}(\mathbf{M}) = \varepsilon_{ij}(0) + \left.\frac{\partial \varepsilon_{ij}}{\partial M_k}\right|_{M_k=0} M_k + \left.\frac{\partial^2 \varepsilon_{ij}}{\partial M_k \partial M_l}\right|_{M_k=0, M_l=0} M_k M_l \,, \tag{3.2}$$

where $\mathbf{M}$ denotes the magnetisation of the material.

When working in special geometries, the general form of the permittivity tensor 3.1 simplifies, since it has to satisfy the Neumann theorem [8] for the symmetry of the given problem. In case of polar geometry (see figure 2.3) one can imagine, that the magnetisation vector $\mathbf{M}$ is generated by a current circulating around it in a loop perpendicular to $\mathbf{M}$. Thus the problem is invariant for any rotation of the Cartesian coordinate system about the magnetisation vector and for any reflection over the magnetisation vector. Therefore the permittivity tensor has to also be invariant to such rotations and reflections. This leads to a form of the permittivity tensor for polar geometry [6]

$$\boldsymbol{\varepsilon}_p = \begin{bmatrix} \varepsilon_{xx} & \varepsilon_{xy} & 0 \\ -\varepsilon_{xy} & \varepsilon_{xx} & 0 \\ 0 & 0 & \varepsilon_{zz} \end{bmatrix} , \tag{3.3}$$

whose components satisfy

$$\varepsilon_{xx}(-M) = \varepsilon_{xx}(M) , \tag{3.4}$$
$$\varepsilon_{zz}(-M) = \varepsilon_{zz}(M) , \tag{3.5}$$
$$\varepsilon_{xy}(-M) = -\varepsilon_{xy}(M) . \tag{3.6}$$

From these equations, we can see that the diagonal elements are even functions of $\mathbf{M}$, while the off-diagonal are odd. For $\mathbf{M} = 0$, the permittivity tensor ε_p is diagonal.
It can be shown, that a restriction to linear magneto-optical effects (i.e. omitting the quadratic term in 3.2) leads to $\varepsilon_{xx} = \varepsilon_{zz}$ and relation 3.3 can be rewritten in a more conventional form

$$\boldsymbol{\varepsilon}_p = \begin{bmatrix} \varepsilon_1 & i\varepsilon_2 & 0 \\ -i\varepsilon_2 & \varepsilon_1 & 0 \\ 0 & 0 & \varepsilon_1 \end{bmatrix} . \tag{3.7}$$

3.1.2 The Lorentz model

One classical theory often used for calculating the permittivity tensor is based on the Lorentz model describing an interaction of an optical electromagnetic wave with harmonically bound electron with a finite relaxation time τ. Using the Lorentz model one can derive the following equations for the permittivity tensor elements 3.3 for an electromagnetic wave propagating along the z axis (in a positive sense) of the Cartesian coordinate system in an external magnetic field $\mathbf{B}_E = (0, 0, -B_z)$ [6]

$$\varepsilon_{zz} = 1 + \omega_p^2 \frac{1}{\omega_0^2 - \omega^2 + i\Gamma\omega} , \tag{3.8}$$
$$\varepsilon_{xx} = 1 + \omega_p^2 \frac{\omega_0^2 - \omega^2 + i\Gamma\omega}{(\omega_0^2 - \omega^2 + i\Gamma\omega)^2 - \omega_c^2\omega^2} , \tag{3.9}$$
$$\varepsilon_{xy} = \omega_p^2 \frac{i\omega\omega_c}{(\omega_0^2 - \omega^2 + i\Gamma\omega)^2 - \omega_c^2\omega^2} , \tag{3.10}$$

where $\omega_c = -eB_z/m$ is the cyclotron frequency, e is charge of the electron, m is mass of the electron, $\omega_p = Ne^2/m\varepsilon_0$ denotes the plasma frequency, ω is the frequency of the propagating electromagnetic wave and $\Gamma = 1/\tau$ is a damping constant.
Equations 3.8, 3.9 and 3.10 exhibit resonance behaviour for specific frequencies ω_0, because of this, such contributions to the permittivity spectra are called *Lorentz oscillators*.

3.1.3 The Drude model

The Drude model describes the free electron contribution to the permittivity. It explains reasonably well a contribution of intraband transitions to the permittivity at low energies. The interband transitions are explored in more detail in [6]. Permittivity elements for the Drude model can be easily obtained from equations 3.8, 3.9 and 3.10 by assuming $\omega_0 = 0$

$$\varepsilon_{zz} = 1 + \frac{\omega_p^2}{-\omega^2 + i\Gamma\omega} , \tag{3.11}$$

$$\varepsilon_{xx} = 1 + \frac{\omega_p^2(-\omega^2 + i\Gamma\omega)}{(-\omega^2 + i\Gamma\omega)^2 - \omega_c^2\omega^2} \tag{3.12}$$

$$\varepsilon_{xy} = \frac{i\omega_p^2\omega\omega_c}{(-\omega^2 + i\Gamma\omega)^2 - \omega_c^2\omega^2} . \tag{3.13}$$

The Drude model contributions to the permittivity spectra often accompany Lorentz oscillators to explain the behaviour at low energies.

3.2 Wave equation in an anisotropic medium

To describe light propagation in materials, it is useful to introduce a *reduced wavevector* $\bar{\mathbf{N}}$, defined as the wavevector $\mathbf{k}$ divided by the magnitude of the wavevector in a vacuum $|\mathbf{k}_0| = \omega/c$

$$\bar{\mathbf{N}} := \frac{c}{\omega}\mathbf{k} = \left(\bar{N}_x\mathbf{i}_x + \bar{N}_y\mathbf{i}_y + \bar{N}_z\mathbf{i}_z\right) . \tag{3.14}$$

The absolute value of the reduced wavevector is equal to the index of refraction

$$\left|\bar{\mathbf{N}}\right| = \frac{c}{\omega}|\mathbf{k}| = \frac{c}{\omega}\frac{\omega n}{c} = n . \tag{3.15}$$

When describing light propagation in an absorbing medium, it is very convenient to use a *complex index of refraction*, with real and imaginary part $n \to n - ik$. To avoid confusion, lets emphasise that in this and later sections, k stands for the imaginary part of the complex index of refraction and not the magnitude of the wavevector $\mathbf{k}$.

One could now derive and solve the wave equation in an absorbing, anisotropic medium without any additional constraints. However, for this thesis, it is sufficient to work with the case of the electromagnetic wave propagating along the direction of the magnetisation vector.
Suppose we have an electromagnetic wave propagating parallel with the z axis of the Cartesian coordinate system and a magnetisation vector oriented in the -$\mathbf{z}$ direction. The permittivity tensor is then given by 3.7 and the reduced wavevector simplifies to

$$\bar{\mathbf{N}} = \left(0, 0, \bar{N}_z\mathbf{i}_z\right) . \tag{3.16}$$

One can then derive an equation for $\bar{N}_z$ in the form [6]

$$\begin{bmatrix} \varepsilon_1 - \bar{N}_z^2 & -i\varepsilon_2 & 0 \\ i\varepsilon_2 & \varepsilon_1 - \bar{N}_z^2 & 0 \\ 0 & 0 & \varepsilon_1 \end{bmatrix} \begin{bmatrix} e_x \\ e_y \\ e_z \end{bmatrix} = 0 . \tag{3.17}$$

For this equation to have a non trivial solution, the determinant must be zero. Its characteristic equation than leads to

$$\bar{N}_z^2 = \varepsilon_1 \pm \varepsilon_2 \,. \tag{3.18}$$

Recalling the definition of the reduced wavevector $\bar{N}$, we can see that $\varepsilon_1 \pm \varepsilon_2$ are squares of the complex refractive indices describing propagation of so called proper modes in the medium

$$N_+ = \sqrt{\varepsilon_1 + \varepsilon_2} \quad \text{and} \quad N_- = \sqrt{\varepsilon_1 - \varepsilon_2} \,. \tag{3.19}$$

The four values N_z solving 3.17 along with their proper modes are summarised in table 3.1. Looking at table 3.1, one can notice, that the proper modes are right (RCP)

$\bar{N}_{z1} = N_+$	$\bar{N}_{z2} = -N_+$	$\bar{N}_{z3} = N_-$	$\bar{N}_{z4} = -N_-$
$e_1 = \begin{bmatrix} 1 \\ i \end{bmatrix}$	$e_2 = \begin{bmatrix} 1 \\ i \end{bmatrix}$	$e_3 = \begin{bmatrix} 1 \\ -i \end{bmatrix}$	$e_4 = \begin{bmatrix} 1 \\ -i \end{bmatrix}$

Table 3.1: summary of solutions to equation 3.17

and left (LCP) circular polarisations introduced in 2.10.
The permittivity tensor elements are complex numbers

$$\varepsilon_1 = \varepsilon_1' - i\varepsilon_1'' \quad \text{and} \quad \varepsilon_2 = \varepsilon_2' - i\varepsilon_2'' \,. \tag{3.20}$$

We can therefore rewrite relationship 3.18 using the complex refractive index $N_\pm = n_\pm - ik_\pm$ as

$$(n_\pm - ik_\pm)^2 = (\varepsilon_1' - i\varepsilon_1'') \pm (\varepsilon_2' - i\varepsilon_2'') \,. \tag{3.21}$$

However, calculating the values of $n_\pm$ and $k_\pm$ from 3.21 can be cumbersome, so in practice one usually expresses the complex refractive indices $N_\pm$ as

$$N_\pm \approx N \pm \Delta N \,, \tag{3.22}$$

where N is the complex refractive index of the optically isotropic medium and ΔN represents the perturbation introduced by the magnetic ordering. Experience shows, that errors introduced by 3.22 are below experimental accuracy [6]. Equations 3.18, 3.21 together with the fact, that $\sqrt{\varepsilon_1} \approx N$ lead to an important relationship

$$\Delta N \approx \frac{\varepsilon_2}{2\sqrt{\varepsilon_1}} = \frac{i\varepsilon_{xy}}{2\sqrt{\varepsilon_{xx}}} \tag{3.23}$$

3.2.1 Polar Kerr effect at normal light incidence

Lets now derive expressions for polar Kerr effect at normal incidence on the surface of a very thick magnetic metal. Considering a reflection of the electromagnetic waves at the interface between vacuum and the magnetic material, one can use Fresnel reflection coefficients and arrive at the following relation [9]

$$r_\pm = -\frac{N_\pm - 1}{N_\pm + 1} \,, \tag{3.24}$$

where $r_\pm$ are reflection coefficients for the circular RCP and LCP polarisations

$$r_+ = r_{ss} + ir_{ps} \quad \text{and} \quad r_- = r_{ss} - ir_{ps} \,. \tag{3.25}$$

Combining equations 2.38, 2.39, 3.24 and 3.25 we obtain

$$\theta_K - i\epsilon_K \approx i\frac{r_+ - r_-}{r_+ + r_-} = i\frac{N_+ - N_-}{N_+N_- - 1} \,, \tag{3.26}$$

which with the help of equation 3.23 leads to

$$\theta_K - i\epsilon_K \approx \frac{i\varepsilon_2}{\sqrt{\varepsilon_1}(\varepsilon_1 - 1)} \,. \tag{3.27}$$

Rewriting ε_1 and ε_2 in 3.27 in terms of their real and imaginary parts and considering $\sqrt{\varepsilon_1} \approx n - ik$, we can express the polar Kerr rotation and ellipticity at a single interface as

$$\theta_K \approx \frac{C\varepsilon_2'' - D\varepsilon_2'}{C^2 + D^2} \,, \tag{3.28}$$

$$\epsilon_K \approx \frac{C\epsilon_2' + D\epsilon_2''}{C^2 + D^2} \,, \tag{3.29}$$

where

$$C = n\left(n^2 - 3k^2 - 1\right) \quad \text{and} \quad D = k\left(3n^2 - k^2 - 1\right) \,. \tag{3.30}$$

From equations 3.28 and 3.29 we can also express ε_2' and ε_2'' as

$$\varepsilon_2' \approx -\left(C\theta_K - D\epsilon_K\right) \,, \tag{3.31}$$

$$\varepsilon_2'' \approx -\left(C\epsilon_K + D\theta_K\right) \,. \tag{3.32}$$

Equations 3.31 and 3.32 are very powerful, because they allow us to calculate the off-diagonal component of the permittivity tensor ε_2 from experimentally measured Kerr angle θ_K, Kerr ellipticity ϵ_K and optical constants of the material n and k.

Chapter 4

Magnetism and magnetic materials

In this chapter, we will take a brief look at the classification of matter according to its magnetic properties. Special attention will be given to ferrimagnets as the materials studied in this thesis belong to this class. We will not focus in detail on the quantum origins of magnetism, as it is beyond the scope of this thesis, but will use quantum formalism when necessary. Namely the exchange interaction will be introduced as the main driving force responsible for different magnetic microstructures. We will also touch on hysteresis loops, how we can measure them with magneto-optic techniques and discuss what they can tell us about the studied materials.

4.1 Categorisation of magnetic materials

There are multiple ways to categorise magnetic substances. In this thesis, magnetic substances will be split into four groups based on their magnetic ordering. The four groups are paramagnetic, ferromagnetic, antiferromagnetic and ferrimagnetic materials. The aforementioned magnetic ordering types are depicted in figure 4.1, where the arrows indicate magnetic moments of the crystal constituents. In case of ferromagnetic ordering, magnetic moments are aligned and the material exhibits spontaneous magnetisation. In antiferromagnetic materials, the neighboring magnetic moments have the same magnitude, but point in the opposite direction. Therefore the total magnetic moment is zero and so such materials are not magnetic and cannot be permanently magnetised by an external magnetic field. In paramagnetic materials, the magnetic moments are randomly oriented again adding up to zero as in case of antiferromagnets. However, contrary to antiferromagnets, in the presence of an external magnetic field the magnetic moments align and the material becomes magnetic. When the field is removed, paramagnetic materials lose their magnetisation. Finally, in ferrimagnetic materials, the neighboring magnetic moments point in the opposite direction, but since the magnitudes of the opposite pointing moments are not equal, they do not completely cancel out and the bulk material exhibits often weak, but non zero magnetisation.
Let us also mention, that this categorisation is not exhaustive. For example one can also introduce diamagnetism, superparamagnetism or the newly discovered altermagnetism.

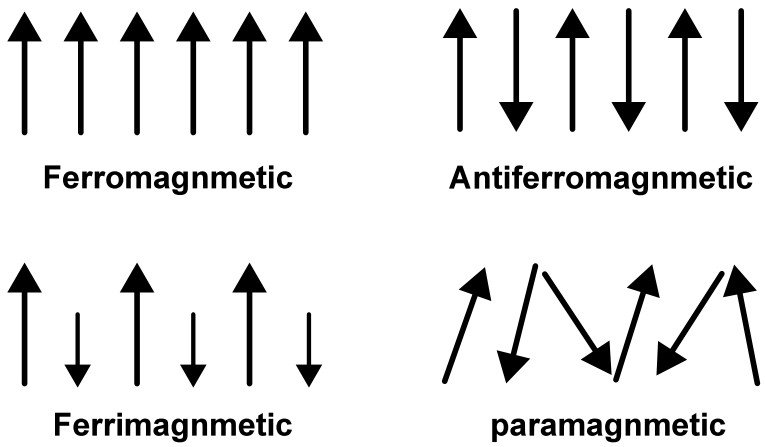

Figure 4.1: Different magnetic ordering categories.

4.2 Ferrimagnetism

As mentioned above, ferrimagnetic materials usually exhibit a net magnetisation moment. Same as in the case of ferromagnetic materials, above a certain temperature called the *Currie temperature*, the material loses its magnetic properties. This is because as the temperature increases, the magnetic moments inside the material start to decouple thanks to the increased thermal energy. Above the Currie temperature, at any point in time, the individual magnetic moments point in essentially random directions and so the net magnetisation is zero. Usually, with increasing temperature, the total magnetisation of the material gets smaller and smaller until it dissapears altogether at the Currie temperature. Same process also applies to ferrimagnetic materials. However, in ferrimagnetic materials, there can exists another temperature, where the magnetic moments cancel out called the *compensation temperature*. In ferrimagnets, sublattices responsible for the opposing magnetic moments often exhibit different temperature dependence. Thanks to this, there can exist a temperature below the Currie temperature where the two opposing moments cancel out leaving the material with zero net magnetisation. This phenomenon is ilustrated in figure 4.2. From the same figure, we can also see that the direction of net magnetisation switches at the compensation temperature.

4.2.1 Exchange interaction

The previous text of this chapter described the basic categorisation of magnetic materials based on their magnetic properties. However, it is still not clear why some materials prefer to have the magnetisation of their sub-lattices oriented in parallel, while others prefer an anti-parallel orientation. An answer lies in quantum mechanics, namely the *exchange interaction*.
Exchange interaction is an interaction between identical particles. To illustrate the mechanism of the interaction, consider a two electron system with no or very weak spin orbit coupling. Disregarding the spin-orbit coupling, the system Hamiltonian $\hat{H}$ is spin-independent. One can then separate the spacial ψ and spin χ part of the wavefunction as

$$\Psi(\mathbf{r}_1, \mathbf{r}_2, s_1, s_2) = \psi(\mathbf{r}_1, \mathbf{r}_2)\chi(s_1, s_2)\,, \tag{4.1}$$

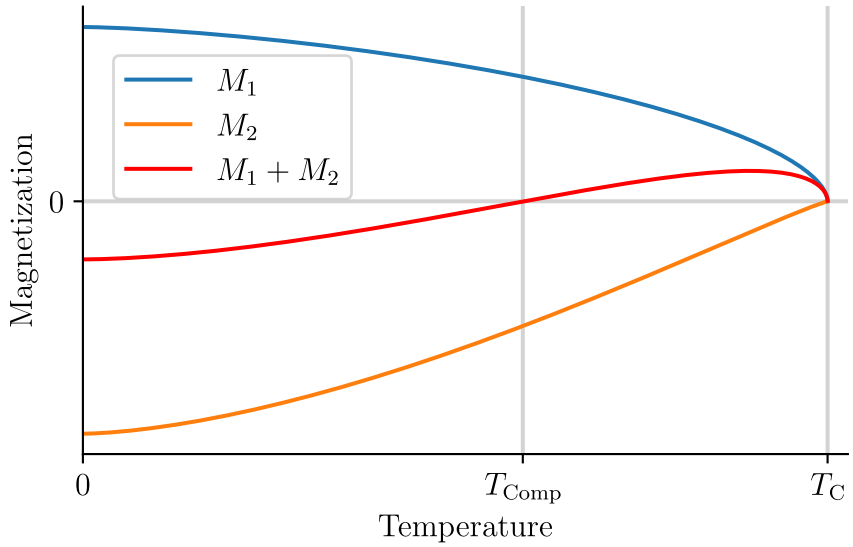

Figure 4.2: Origins of the compensation temperature in ferrimagnets from different magnetization temperature dependence M_1, M_2 of individual crystal sublattices.

where $\mathbf{r}_1, \mathbf{r}_2$ and s_1, s_2 describe the position and spin state of the two electrons respectively. The orbital eigen functions satisfying

$$\hat{H}\psi = E\psi \tag{4.2}$$

are also spin-independent along with their energy states, thanks to the spin-independence of the Hamiltonian. However, since electrons are fermions, Pauli's exclusion principle needs to be satisfied and so the wavefunction 4.1 must be anti-symmetric. It is well known, that a system consisting of two particles with spin $1/2$ can have four possible spin states χ, one anti-symmetric with with a total spin $S = 0$ called the *singlet state* and three symmetric states with the total spin $S = 1$ called *triplet states*. From equation 4.1 and the Pauli's exclusion principle, it is clear that the spacial wavefunction ψ has to be symmetric when the spin wavefunction χ is anti-symmetric or anti-symmetric when χ is symmetric. Because of this, the orbital eigenfunctions of the Hamiltonian have to be different for electrons with parallel spins ($S = 1$ and χ is symmetric so ψ must be anti-symmetric) and for electrons with anti-parallel spins ($S = 0$ and χ is anti-symmetric so ψ must be symmetric). Since the energy states depend on ψ (see 4.2), they also depend on the spin state of the two electrons. This energy dependence is the origin of the exchange interaction. In practise, for multi-particle systems, this effective interaction of the magnetic moments is approximately given by the following Hamiltonian [10]

$$\hat{H}_{spin} = -J_{ij}\mathbf{S}_i \cdot \mathbf{S}_j \,, \tag{4.3}$$

where $\mathbf{S}_i$ and $\mathbf{S}_j$ are the spin operators of the i-th and j-th particles and J_{ij} is the exchange integral defined as

$$J_{ij} = \int d^3\mathbf{r}_i d^3\mathbf{r}_j \frac{\psi_i^*(\mathbf{r}_i)\psi_j(\mathbf{r}_i)\psi_j^*(\mathbf{r}_j)\psi_i(\mathbf{r}_j)}{|\mathbf{r}_i - \mathbf{r}_j|} \,. \tag{4.4}$$

Equation 4.3 can be generalised as a sum over all neighbouring particles/atoms

$$\hat{H}_{spin} = -\sum_{i,j} J_{ij}\mathbf{S}_i \cdot \mathbf{S}_j \,. \tag{4.5}$$

The sign of J indicates magnetic ordering. When the exchange integral is positive $J > 0$, neighbouring spins tend to align in parallel leading to a ferromagnetic structure. When the exchange integral is negative $J < 0$ neighbouring spins tend to point in the opposite direction leading to an anti-ferromagnetic or ferrimagnetic ordering.

4.3 Hysteresis loops

The magnetization value of the magnetically ordered materials depends on the history of an applied external magnetic field. Such property is called *hysteresis*. By applying an external magnetic field and measuring the material magnetisation M for different field strengths we can construct a *hysteresis loop* depicted in figure 4.3. In this section, for simplicity, we will describe hysteresis loop typical for a ferromagnetic material. In ferromagnetic materials, the material is composed of a number of magnetic *domains* with parallel magnetisation vectors. Magnetic moments of different domains generally point in different directions resulting in hysterical behavior.
We start with a non-magnetised ferromagnetic material and no external magnetic field (i.e magnetisation vectors of the domains are oriented randomly). When introducing and raising the external magnetic field, the domains inside the material start to align with the magnetic field and total magnetisation increases. When all magnetic moments of all the domains are aligned, the magnetisation can no longer increase even for a stronger magnetic field. We have reached a magnetic saturation point M_{sat}. If we now start to lower the external magnetic field all the way to zero, we notice the magnetisation decreasing, as the magnetic moments of the domains start to partially point in different directions. However, even with no external magnetic field present, there remains a nonzero magnetisation called the *remanence magnetisation* M_r. Increasing the field in the opposite direction begins to reorient the domains and the total magnetisation reaches 0 for the *coercive field* H_c. If we increase the field further, the magnetisation again saturates at $-M_{sat}$. The field strength needed to reach the saturation point and the slope with witch the saturation point is reached depends on the material and its magnetic structure.

Because the linear magneto-optic Kerr effect is directly proportional to the magnetisation of the measured sample, it can be used to construct hysteresis loops where we have the Kerr rotation angle instead of the magnetisation on the y axis. However, the Kerr rotation also exhibits spectral dependence so only the shape of the MOKE hysteresis loop coincides with magnetisation hysteresis loop but not its magnitude.

4.4 Magnetic anisotropy

Some materials are easier or harder to magnetise depending on their crystallographic orientation with respect to the external magnetic field. The axis along which the material magnetises the easiest is called the *easy axis*. The remanence value of the material when magnetised along this axis is grater than if it was magnetised along any other axis. Perpendicular to this axis lies the *hard axis*. When magnetising along the hard axis, the magnetic moments are less prone to orient along the external field. When the external field is removed, the remaining remanence value is generally minimal. The field value needed to reach saturation along the hard axis is called the anisotropy field. The difference in hysteresis loops when measuring along the easy and hard axis

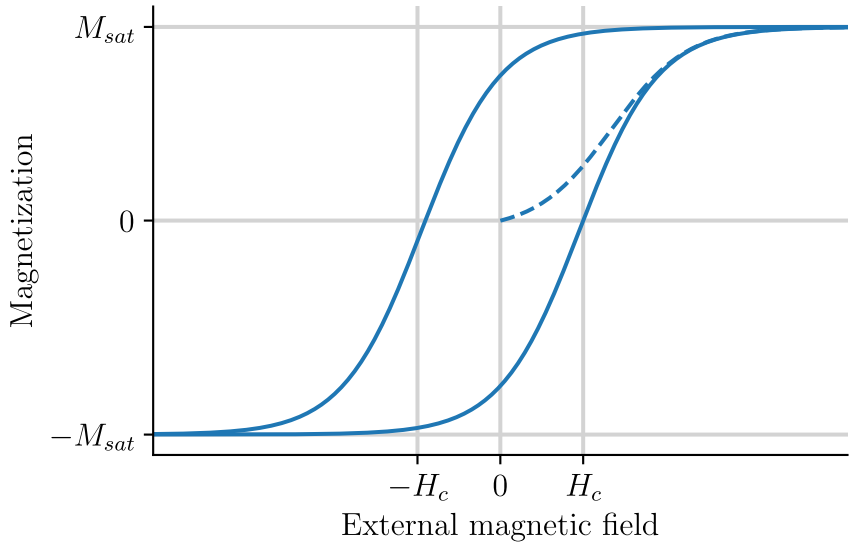

Figure 4.3: Hysteresis loop of a ferromagnetic material.

is illustrated in figure 4.4.

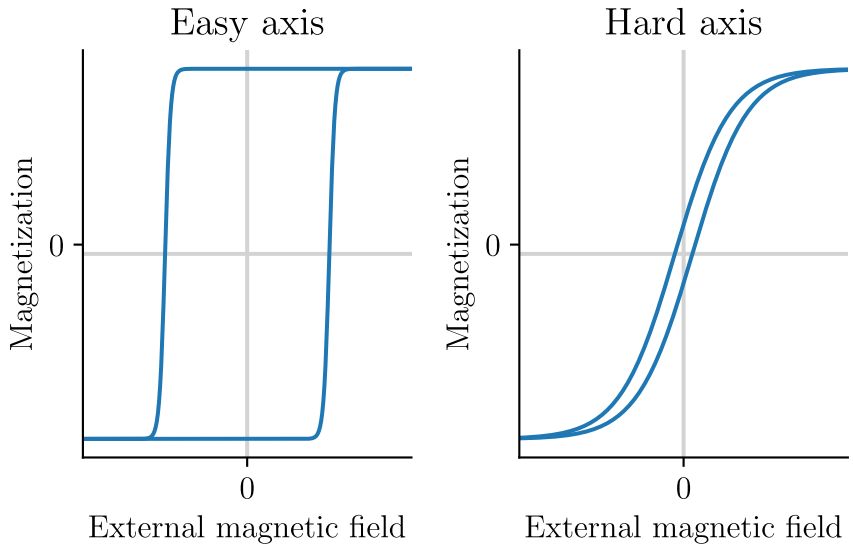

Figure 4.4: Hysteresis loops with external field along the easy and hard axis

As mentioned before, we can use MOKE measurements to construct hysteresis loops. However, one has to keep in mind, that the measured MOKE hysteresis loop is proportinal to the total magnetisation of the sample. When the sample consists of multiple magnetic sublattices with different coercive field values, such is often the case in ferrimagnetic materials, the measured hysteresis loop may appear anomalous. The situation is ilustrated in figure 4.5 for two sublatices with opposite magnetisation vectors of unequal amplitudes (i.e - for a ferrimagnetic material). The different contributions of individual sublattices can often be resolved and separated.

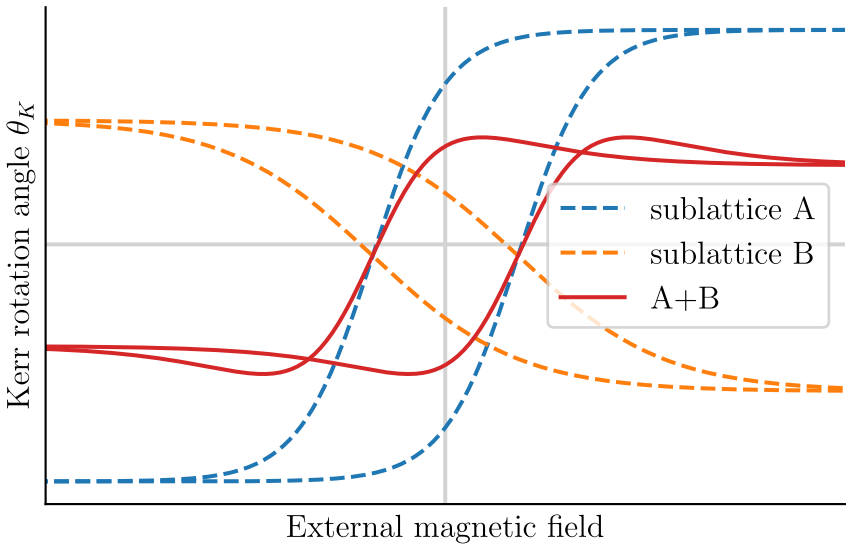

Figure 4.5: Anomalous MOKE hysteresis loop as a sum of MOKE spectra of two sublattices

Chapter 5

Experimental techniques

This chapter focuses on experimental setups used to measure observable variables introduced in previous chapters. Namely *Spectroscopic ellipsometry* and *Magneto-optical spectroscopy* will be discussed for measuring parameters related to the diagonal and off diagonal elements of the permittivity tensor respectively.

5.1 Spectroscopic ellipsometry

Spectroscopic ellipsometry is a non destructive optical technique for investigating the optical response of materials. As opposed to single-wavelength ellipsometry, spectroscopic ellipsometry employs a wide-range light source allowing its use for reconstructing the diagonal permittivity tensor element function for a broad spectrum of wavelengths. The experimental setup used for such measurements is schematically depicted in figure 5.1. The light is generated by a light source S, it than passes through a linear polariser P, before reflecting off of the sample. After reflecting from the sample, the light continues first through a compensator C, than through an analyzer A, after which it finally reaches the detector D.

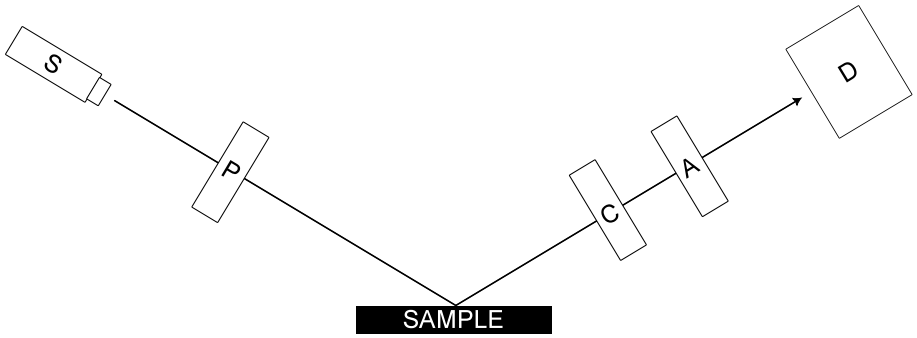

Figure 5.1: Experimental spectroscopic ellipsometry setup: light source S, polariser P, compensator C, analyzer A, detector D

Using the orthogonal s and p polarisation basis introduced in the previous chapters, the Jones transmission matrix for the linear polariser at angle ξ with respect to the x axis can be described as

$$\mathbf{P} = \begin{bmatrix} \cos^2\xi & \sin\xi\cos\xi \\ \sin\xi\cos\xi & \sin^2\xi \end{bmatrix} . \tag{5.1}$$

The polarisation change stemming from the reflection off the sample is characterised by the Jones reflection matrix $\mathbf{R}_{sp}$ defined in 2.15. Assuming optically isotropic sample, the off-diagonal elements, as discussed before, disappear and one is left with

$$\mathbf{R}_{sp} = \begin{bmatrix} r_{ss} & 0 \\ 0 & r_{pp} \end{bmatrix} . \tag{5.2}$$

Next, the light passes through a compensator C. Transmission Jones matrix for an unrotated compensator is

$$\mathbf{C} = \begin{bmatrix} e^{i\Gamma} & 0 \\ 0 & 1 \end{bmatrix} , \tag{5.3}$$

where Γ is the relative phase difference (retardance) induced by the compensator. However, in general, the compensator fast axis is rotated by an angle φ relative to the x axis. We get the Jones transmission matrix for the rotated compensator $\mathbf{C}'$ by rotating the coordinate system by an angle φ with the use of 2.13 and 2.11

$$\begin{aligned} \mathbf{C}' = \mathbf{R}(\alpha)\mathbf{C}\mathbf{R}^{-1}(\alpha) = \begin{bmatrix} \cos\varphi & -\sin\varphi \\ \sin\varphi & \cos\varphi \end{bmatrix} \begin{bmatrix} e^{i\Gamma} & 0 \\ 0 & 1 \end{bmatrix} \begin{bmatrix} \cos\varphi & \sin\varphi \\ -\sin\varphi & \cos\varphi \end{bmatrix} = \\ = \frac{sin(2\varphi)}{2} \begin{bmatrix} \cot(\varphi)e^{i\Gamma} - 1 & e^{i\Gamma} + \cot\varphi \\ e^{i\Gamma} - 1 & \tan(\varphi)e^{i\Gamma} + \cot\varphi \end{bmatrix} . \end{aligned} \tag{5.4}$$

The analyser is another linear polariser oriented at an angle β measured from the x axis. Its Jones transmission matrix is the same as for the first linear polariser 5.1 except with the angle β

$$\mathbf{A} = \begin{bmatrix} \cos^2\beta & \sin\beta\cos\beta \\ \sin\beta\cos\beta & \sin^2\beta \end{bmatrix} . \tag{5.5}$$

The effect of the whole setup including the sample on the polarisation state can in accordance with 2.26 be described by

$$\mathbf{X}_F = \mathbf{A}\mathbf{C}'(\varphi)\mathbf{R}_{sp}\mathbf{P} . \tag{5.6}$$

Assuming the polarisation state of the light generated by the light source S can be described by the Jones vector $\mathbf{J}_{IN}$, the polarisation state of the light entering the detector can than be described by the Jones vector $\mathbf{J}_{OUT}$ where

$$\mathbf{J}_{OUT} = \mathbf{X}_F\mathbf{J}_{IN} . \tag{5.7}$$

The intensity of light entering the detector can be determined by

$$I = (\mathbf{J}_{OUT})^{+}(\mathbf{J}_{OUT}) , \tag{5.8}$$

where the $^{+}$ indicates a Hermitonian transpose. This experimental technique utilises a rotating compensator and fixed polarisers, as seen above. Thanks to that, the setup is able to obtain the ellipsometric parameters Ψ and Δ related to the ratio ρ between r_{pp} and r_{ss} coefficients

$$\rho = \frac{r_{pp}}{r_{ss}} = \tan(\Psi)e^{i\Delta} . \tag{5.9}$$

The ellipsometric parameters Ψ and Δ can be extracted from the intensity 5.7. The exact procedure is quite complicated and can be found in [11].
From spectral measurements of the ellipsometric parameters, optical properties of the sample can be determined. Namely, one can calculate the refraction index n and the extinction coefficient k. From these parameters, the diagonal element of the permittivity tensor ε_1 can be calculated as shown in previous sections.

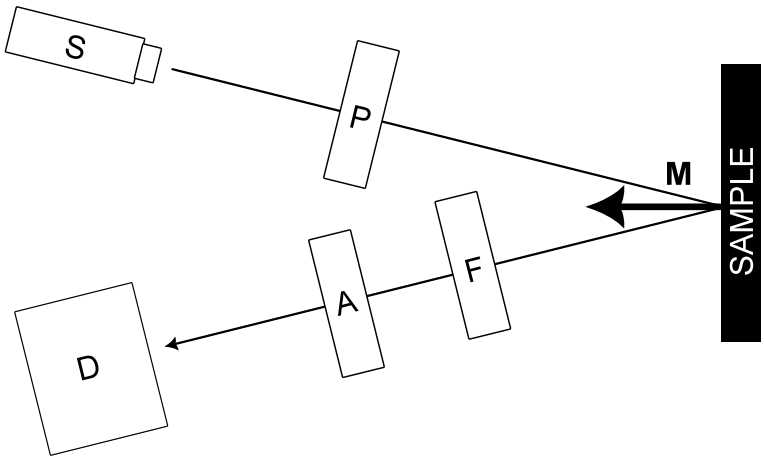

Figure 5.2: Experimental setup for MOKE measurements in polar geometry: light source S, polariser P, phase plate F, analyzer A, detector D, magnetisation $\mathbf{M}$

5.2 Magneto-optical spectroscopy

The experimental setup for magneto-optical (MO) spectroscopy is very similar to the spectroscopic ellipsometry setup. The main difference between the two is the presence of an external magnetic field in the case of magneto-optical spectroscopy. Also, in the case of magneto-optical spectroscopy, the analyzer is able to be rotated during the measurement - *rotating analyzer*. In practice magneto-optical spectroscopy is often performed for small angles of incidence (up to $5°$), because of that it can with very good accuracy be considered to be at normal incidence, which greatly simplifies calculations (see previous chapters). The experimental setup is schematically depicted in figure 5.2.

Similarly to spectroscopic ellipsometry, the light is generated by a light source S. It first passes through a polariser P, whose Johns matrix $\mathbf{P}$ is given by 5.1 and then reflects off of the sample. In the case of magneto-optical spectroscopy, however, the sample isotropy is disturbed by the external magnetic field and so the Jones reflection matrix of the sample is no longer diagonal. The reflection matrix $\mathbf{R}_{sp}$ is, in the case of MO spectroscopy in polar configuration, given by

$$\mathbf{R}_{sp} = \begin{bmatrix} r_{ss} & r_{sp} \\ r_{sp} & -r_{ss} \end{bmatrix} = \begin{bmatrix} 1 & -\phi_K \\ \phi_K & -1\,, \end{bmatrix} \tag{5.10}$$

where we used equation 2.15, relationships 2.34 and 2.35 valid for polar geometry and the definition of the complex Kerr angle 2.38 along with relationship 2.36.

After reflecting off the sample, the light propagates through a phase plate F. Phase plate is just a different name for an optical compensator and so the Jones matrix of the phase plate is accordingly given by 5.3, where Γ is again the induced phase difference. Finally, the light passes through an analyzer A represented by the Jones matrix introduced in 5.5. With the help of relationship 2.26, we can write an equation linking the Jones vector describing the polarisation state of the light entering the detector $\mathbf{J}_{OUT}$ with the Jones vector describing the polarisation state of the light generated by the light source $\mathbf{J}_{IN}$

$$\mathbf{J}_{OUT} = \mathbf{AFR}_{sp}\mathbf{PJ}_{IN}. \tag{5.11}$$

Solving 5.11 with the help of 5.8 ,while assuming that the polariser P defines the incident wave as p-polarised, ($\alpha = 90°$) yields

$$I = \sin^2\beta + |\phi_K|^2 \cos^2\beta + \sin 2\beta \,\mathrm{Re}\Big\{\phi_K e^{i\Gamma}\Big\} \,. \tag{5.12}$$

The value of ϕ_K is usually very small, which was used already when deriving 2.39, so the second order term $|\phi_K|^2$ in 5.12 can be neglected. Minding that and using 2.39 along with the Euler formula, we can rewrite 5.12 as

$$I \approx \sin^2\beta + (\theta_K \cos\Gamma + \epsilon_K \sin\Gamma)\sin(2\beta) \,. \tag{5.13}$$

If we measure the intensity as a function of the angle β, we can use equation 5.13 to fit the measured data and obtain either the Kerr rotation angle θ_K or the ellipticity angle ϵ_K depending on the used phase plate ($\Gamma = 0°$ for Kerr rotation and $\Gamma = 90°$ for ellipticity). To subtract optical contributions of non-magnetic origin, we perform the measurement for a magnetic field $\mathbf{H}$ and $-\mathbf{H}$. Because the Kerr effect is odd in $\vec{B}$, but the background stays roughly the same, we can largely reduce it by using $\theta_K(H) = [\theta_K(H) - \theta_K(-H)]/2$. By background we mainly mean parasitic contributions from from used optical elements (this procedure also removes the quadratic MO Kerr effect).

As mentioned above, theoretically ellipticity could be extracted from intensity spectrum measured with a phase plate satisfying $\Gamma = 90°$. In reality, however, no phase plate can deliver constant retardance throughout a broad spectrum. To obtain ellipticity data, one first measures the Kerr rotation angle θ_K (which is easy, since to obtain $\Gamma = 0$ we just remove the phase plate from the experimental setup) and then performs another measurement with a phase plate of known retardance Γ (including its spectral dependence) and fits the obtained data as a function of β with a constant parameter $(\theta_K \cos\Gamma + \epsilon_K \sin\Gamma)$. Since θ_K is known, ϵ_K can be easily extracted from the fit result.

Chapter 6

Physical properties of Mn_4N

This chapter discusses the crystal and magnetic structure of bulk Mn_4N and proposed magnetic structure of Mn_4N thin films along with other properties. It also mentions doping of Mn_4N with various elements, with a special focus on gallium.

6.1 Structural and magnetic properties of bulk Mn_4N

Mn_4N is a transition metal nitride with antiperovskite structure depicted in figure 6.1. It is a ferrimagnet with antiferromagnetically coupled sub-lattices with the corner magnetic moment about 4 times stronger than the three antiparallel face center moments [12]. Mn_4N has a relatively high Curie temperature of ≈ 740 K [13].

It has long been known, that bulk Mn_4N exhibits (111) magnetic anisotropy [13]. In case of Mn_4N thin films a perpendicular magnetic anisotropy (PMA) is observed as a result of tensile distortion [14] and so the magnetic anisotropy shifts from (111) to (001). Authors of [14] also conclude, that the PMA can be somewhat controlled by the ratio of the perpendicular lattice constant to the in-plane lattice constant (c/a) which can be influenced by the used substrate.
The saturation magnetisation of Mn_4N thin films depends on the method of growth, growth parameters, used substrate and thickness, but usually lies somewhere between 50 kA/m and 200 kA/m [3].

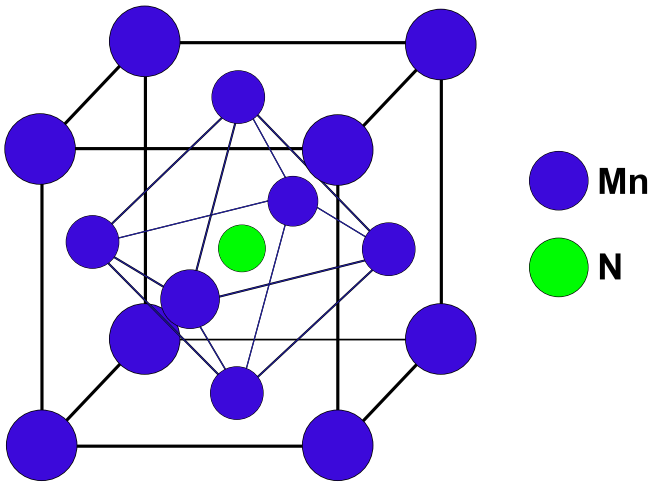

Figure 6.1: Crystal structure of bulk Mn_4N

6.2 Possible ferrimagnetic structures of Mn_4N thin films

Currently there are three main possible ferrimagnetic structures that could theoretically be present in Mn_4N thin films. These proposed structures are depicted in figure 6.2. Bulk Mn_4N has a ferrimagnetic structure depicted in figure 6.2(b) [3]. For thin films, all ferimagnetic structures from figure 6.2 are currently being considered. The author of [2] concludes from comparing theoretical calculations with measured MOKE spectra, that FIM_b phase with a mix of ncFIM phase (see figure 6.2) maight be present in Mn_4N thin films.

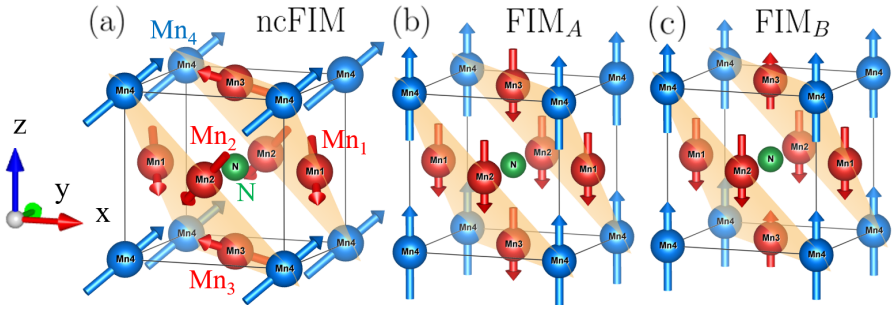

Figure 6.2: Proposed ferrimagnetic structures ncFIM, FIM_A and FIM_B for Mn_4N thin films. Reprinted from [2] and used with the permission of the author.

6.3 Doping of Mn_4N

Doping Mn_4N with other elements can drastically change its magnetic properties. In the past, researchers tried using elements such as Ni, Cr, Fe, In and Sn as replacements for some or all the Mn atoms in Mn_4N with the aim of shifting the compensation point to various temperatures [3]. Such research proves, that it is possible to tune the compensation temperature this way. Recently, nonmagnetic Ga was also tried as a doping element for Mn_4N thin films [15]. Authors of this study conclude, that there is evidence for ferrimagnetic to ferromagnetic transition at higher Ga concentrations. Gallium in Ga doped M_4N occupies the corner positions for low concentrations [16] and appears to occupy the face center positions for higher concentrations ($Mn_{3.5}Ga_{0.5}N$) [15].

Chapter 7

Experimental results

7.1 Investigated samples

The studied samples were provided by Trinity College Dublin, along with the information about their structure summarised in figure 7.1. For this thesis, the layer of interest is the Mn_4N layer. For samples 1 and 2, the Mn_4N layer consist of pure Mn_4N, for samples 3,4 and 5, the Mn_4N layer consists of gallium doped $Mn_{4-x}Ga_xN$ with x =0.11, 0.20 and 0.27 respectively. As can be seen, the main difference between samples 1 and 2 is the substrate.

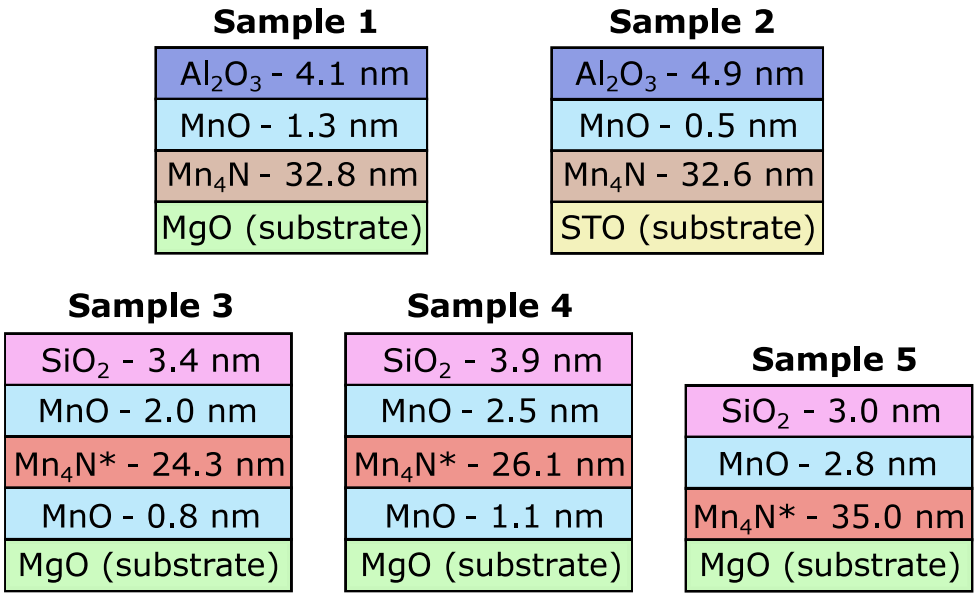

Figure 7.1: Structure of the provided samples. *Gallium doped Mn_4N

7.2 Ellipsometric measurements

All samples were characterised using spectroscopic ellipsometry described more closely in section 5.1. All measurements were done at room temperature using Mueller matrix ellispometer J.A.Woollam RC2 with dual rotating-compensator. Proprietary Software *CompleteEASE* by J.A. Woollam was used both to control the measurement setup and to extract optical information from measured ellipsometric angles. CompleteEASE

enables a user to define a multilayered sample structure and assign optical properties of materials to individual layers using its library of tabulated data. Making use of the known sample structure shown in figure 7.1, we created the appropriate layers in CompleteEASE with assigned thicknesses and optical properties. Lorentz oscillators were then used to parametrise optical dispersion (spectral dependence of optical properties) of the unknown Mn_4N layer by fitting the experimental spectra of ellipsometric angles. The obtained data of the real and imaginary diagonal permittivity tensor elements are plotted in figure 7.2. It is important to note here, that this procedure is only an approximation of the real sample, since it considers only perfectly planar interfaces between layers. The real sample structure may differ from the clear layers illustrated in figure 7.1, mainly by the layer transitions (including the transition of the top layer and air) not being completely smooth, as shown in the figure, but rather having a certain roughness influencing the samples interaction with light and as a result the measured ellipsometric angles. Although the CompleteEASE software allows for including layer roughnesses in the analysis procedure, this requires at least approximate information about the individual layer roughnesses and often does not offer more satisfactory results. Because of this, it was not used during the analysis process. Still the obtained optical properties should not deviate largely from their real values.

Looking at figure 7.2, we can clearly see that the spectra for the two samples of non-doped Mn_4N (samples 1 and 2) look very similar. To better resolve differences between measured spectra, we plot numerically calculated second derivatives in figure 7.3. Looking at the second derivative of the imaginary part $\mathrm{Im}\{\varepsilon_1\}$, there is a spectroscopic structure located near 2.2 eV in case of the the two non-doped samples. This feature is not visible in the spectra of the doped samples suggesting an existence of an electron transition with such energy linked to the corner Mn atoms. As these atoms are being substituted by the Ga atoms, this spectral feature seems to be suppressed, or shifted to lower energies for the doped samples.

The slight observed difference between spectra of the two non-doped samples could be explained by their different substrates. The substrates STO and MgO have different lattice constants (i.e different lengths between atoms in their crystal structure) leading to a different *lattice mismatch* between the substrate and the Mn_4N layer. The lattice mismatch of Mn_4N and MgO is about -7.6 %, while for Mn_4N and STO, the lattice mismatch is only about -0.4 % [17]. This mismatch influences the growth of the Mn_4N layer and causes strain in the sample influencing its optical properties.

In case of the Ga doped samples (samples 3, 4 and 5) we observe different spectral dependencies for each sample, with the samples 3 and 4 being more similar to each other compared to sample 5. This is especially noticeable in the spectra of the real part $\mathrm{Re}\{\varepsilon_1\}$. In the spectra of the imaginary part $\mathrm{Im}\{\varepsilon_1\}$ of sample 3, there appears to be a wide peak at about 3 eV. This bump appears to shift to lower energies in case of sample 4 and is no longer visible in spectra belonging to sample 5 (which might mean it was overlaid by Drude contribution of free electrons). This bump might suggest the presence of a Lorentz oscillator being influenced by the concentration of gallium atoms in the sample. Similar behavior can be seen in the second derivative of the imaginary part $\mathrm{Im}\{\varepsilon_1\}$, where a local minimum starting at approximately 3.3 eV in case of sample 3 appears to shift to about 2.6 eV for sample 4 and is not visible at all for sample 5. Analogously in the second derivative of the real part $\mathrm{Re}\{\varepsilon_1\}$, there appears to be a local maxima at around 4.5 eV in case of sample 3 shifting to about 3.3 eV for sample 4 and to approximately 1.9 eV for sample 5.

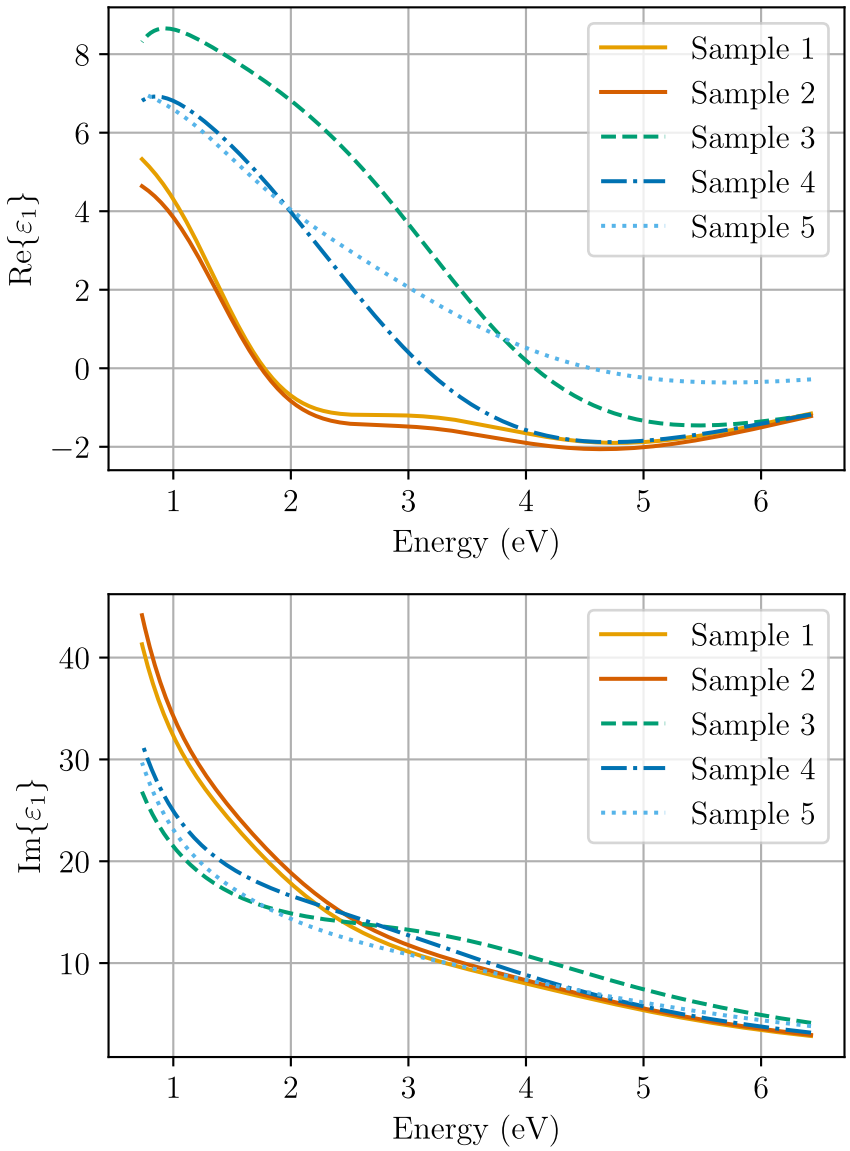

Figure 7.2: Real and imaginary part of the diagonal permittivity tensor elements ε_1 obtained by fitting the spectroscopic ellipsometry measurements with Lorentz oscillators using the CompleteEASE software

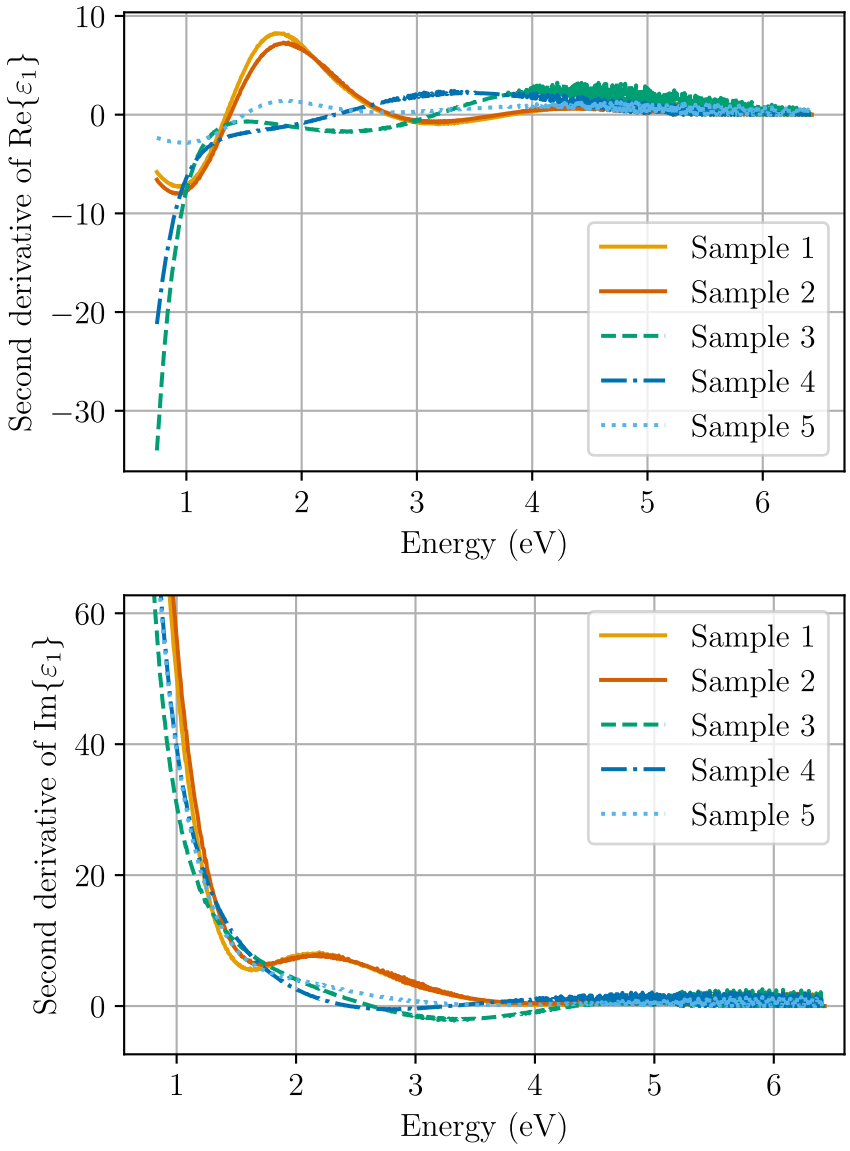

Figure 7.3: Second derivative of the real and imaginary part of the diagonal permittivity tensor elements ε_1 from figure 7.2.

7.3 Kerr rotation and ellipticity

To study magnetic properties and potentially obtain information about the off-diagonal permittivity tensor components, Kerr rotation and Kerr ellipticity spectra of the studied samples at room temperature were measured. Magneto-optical spectroscopy, explained in section 5.2, was used to measure the experimental data and a custom python script was then used to calculate the Kerr rotation and ellipticity spectra for measured energies from 1.3 to 6 eV. As discussed in section 5.2 the Kerr spectra were measured for an external field $B = +1$ T and $B = -1$ T and then subtracted and divided by 2 to get rid of the parasitic background effects. The obtained Kerr rotation and ellipticity spectra can be seen in figure 7.4. The measured spectra for the non-doped samples are again very similar with differences likely caused by the different substrate and thus strain in the samples. Kerr rotation spectra for both non-doped samples show a clear peak between 2 and 3 eV agreeing nicely with a spectral feature observed at similar energies in the second derivative of the imaginary part $\mathrm{Im}\{\varepsilon_1\}$.
As for the Ga doped samples, we can see that for samples 3 and 4, the measured Kerr rotation and ellipticity angles are very small. This is likely caused by the relative proximity of the compensation temperature of these samples to room temperature. As can be seen from figure 4.2, near the compensation temperature, net magnetisation is comparatively small. Furthermore, the field needed to reach magnetic saturation of these samples at room temperature may be larger than the 1 T used, further lowering the observed MOKE magnitude. As for sample 5, the magnitude of the measured MOKE spectrum is comparatively greater, likely as a result of the compensation temperature shifting further away from the room temperature. Furthermore, the measured Kerr rotation spectra for sample 5 does *not* cross zero unlike other samples.
It is important to note the sign reversal between the measured spectra for samples 3 and 4. This observation agrees nicely, with the observed sign reversal between Ga concentrations of $x = 0.1$ and $x = 0.3$ in literature [15]. The sign reversal between these two samples indicates that the compensation temperature is greater then the room temperature for one of the samples and lower then the room temperature for the other sample. Since pure Mn_4N has a compensation temperature of around 500 K [18], noting that the MOKE sign is the same for pure Mn_4N (samples 1 and 2) and for $Mn_{3.89}Ga_{0.11}N$ (sample 3), we can conclude that $Mn_{3.89}Ga_{0.11}N$ has a compensation temperature above room temperature, while $Mn_{3.80}Ga_{020}N$ (sample 4) and $Mn_{3.73}Ga_{0.27}N$ (sample 5) have compensation temperatures below the room temperature.

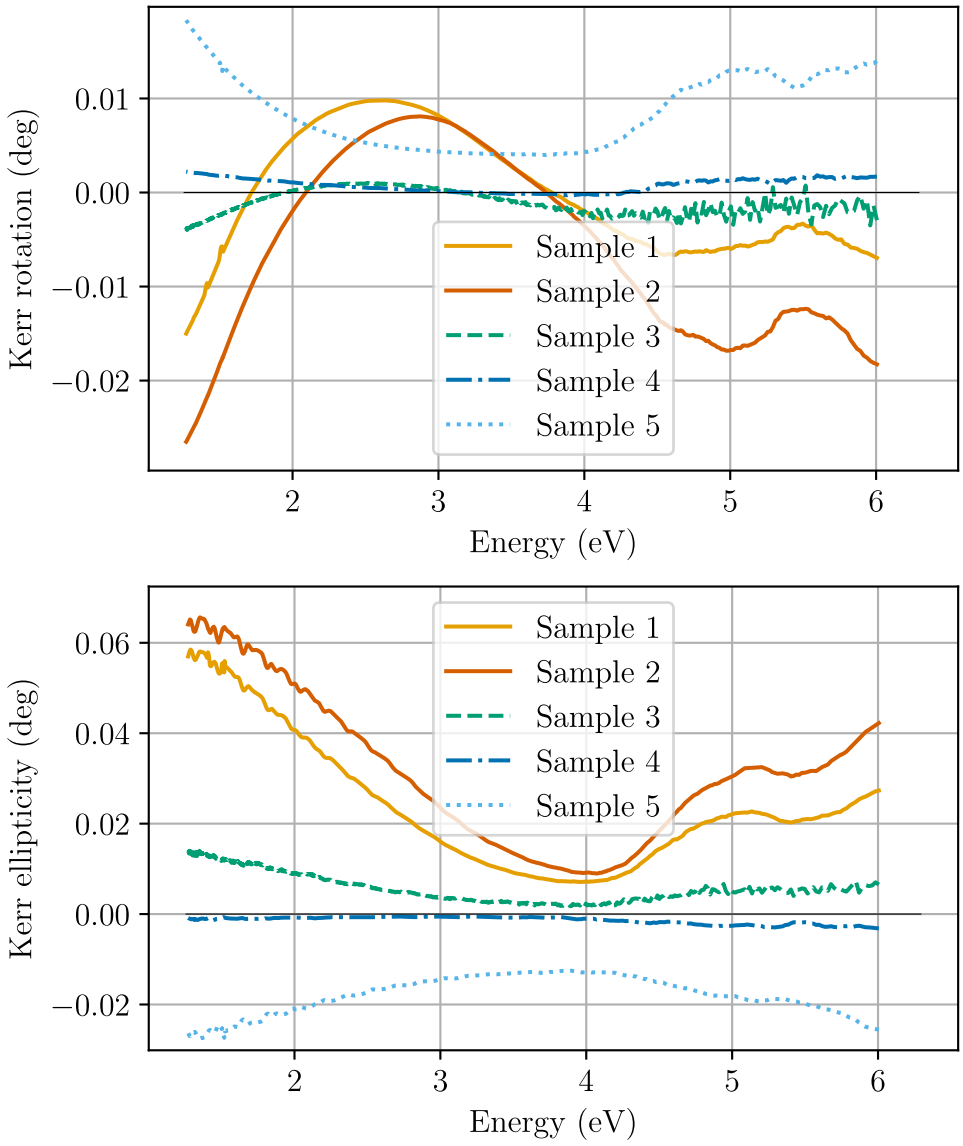

Figure 7.4: Obtained Kerr rotation and ellipticity spectra of the studied samples

7.3.1 Comparison of measured and theoretically calculated MOKE spectra for pure Mn_4N films

For the two non-doped samples, theoretical Kerr rotation and ellipticity spectra for proposed ferrimagnetic phases ncFIM, FIM_A and FIM_B from figure 6.2 were calculated. Material data for the Mn_4N layer obtained by DFT calculations (i.e the individual ferrimagnetic phases) were adapted from [2]. Yeh matrix formalism was then used to simulate MOKE spectra for our samples respecting the known sample structure from figure 7.1. These simulations were done separately for each phase and assumed the Mn_4N layer to be made entirely out of one of these ferrimagnetic phases. The calculated MOKE spectra for individual phases for sample 2 are shown in figure 7.5. The calculated MOKE spectra for sample 1 are slightly different because of the different substrate. However, as the difference is small, they are not plotted separately in this thesis. Note that the theoretical simulations of the material parameters [2] used for

the theoretical MOKE calculations were performed for temperature of 0 K and an infinite perfect crystal lattice. The experimental MOKE measurements were done at room temperature on thin film samples. As a result, the spectral characteristics visible in 7.5 get smeared greatly by thermal fluctuations and crystal imperfections. Comparing figures 7.4 and 7.5 the best agreement can be found for FIM_A (note that we are compering only spectral dependencies and disregard the magnitude or the sign as they can be influenced by the way the experiment is performed). However, it may be possible to obtain even better agreement by mixing the FIM_A and the ncFIM phase together. An attempt at this is illustrated in figure 7.6. Here we obtained the mixed spectrum M simply by adding the two phases together while moderating them by parameters A, B and total amplitude parameter K as

$$M = K(A \cdot FIM_A + B * \cdot ncFIM) \,. \tag{7.1}$$

The "optimal" values of A and B were found by manually moderating them and judging the agreement between theoretical and measured spectra by eye as analytical fitting would not offer satisfactory results due to numerical instability. This is because we would have to account for the temperature and crystal imperfection smearing of the theoretical data and because more importance is assigned to some spectral characteristics like where the spectra cross zero. The "optimal" values of A and be B used in figure 7.6 were determined as $A = 1.69$, $B = 2.58$ in case of sample 1 and $A = 1.53$, $B = 2.92$ in case of sample 2. The absolute values of these parameters are not important, as the spectrum is additionally scaled by a total amplitude parameter K (in this case $K = -0.02$ was used for both samples). What is important is the ratio of the two parameters A and B mimicking the theoretical ratio of the two phases in the samples. Calculating this, we get $A/B = 0.66$ for sample 1 and $A/B = 0.52$ for sample 2. Interestingly enough, although the ncFIM phase does not offer great agreement with experimental data on its own, when mixed with some FIM_A phase, the agreement with experiment might be even better than the pure FIM_A phase.
However, it is important to interpret these results purely as a suggestion that the coexistence of the two phases may give rise to a better agreement with measured data. *The described procedure offers only qualitative and not 100 % conclusive results.*
For both the pure FIM_A phase and the mix of phases FIM_A and ncFIM, the theoretical and experimental Kerr rotation spectra are roughly in agreement only between about 1.6 and 4.2 eV. For lower and higher energies, the agreement is considerably worse. In the case of low energies the disagreement is expected, as explained in source literature [2], due to intraband transitions, which are not considered in the DFT calculations of material parameters. In the case of high energies, it is unclear what causes the observed discrepancy. Furthermore, the Kerr ellipticity spectra is roughly in agreement only in terms of the overall shape, however, experimental spectra seems to be shifted upwards (to larger angles) compared to the theoretical spectra. This can not be accounted for by simple total amplitude scaling as the theoretical spectra crosses 0 but the experimental spectra does not. None of the three proposed ferrimagnetic phases lead to purely positive ellipticity spectra and it is unclear what causes the observed shift in experimental data.

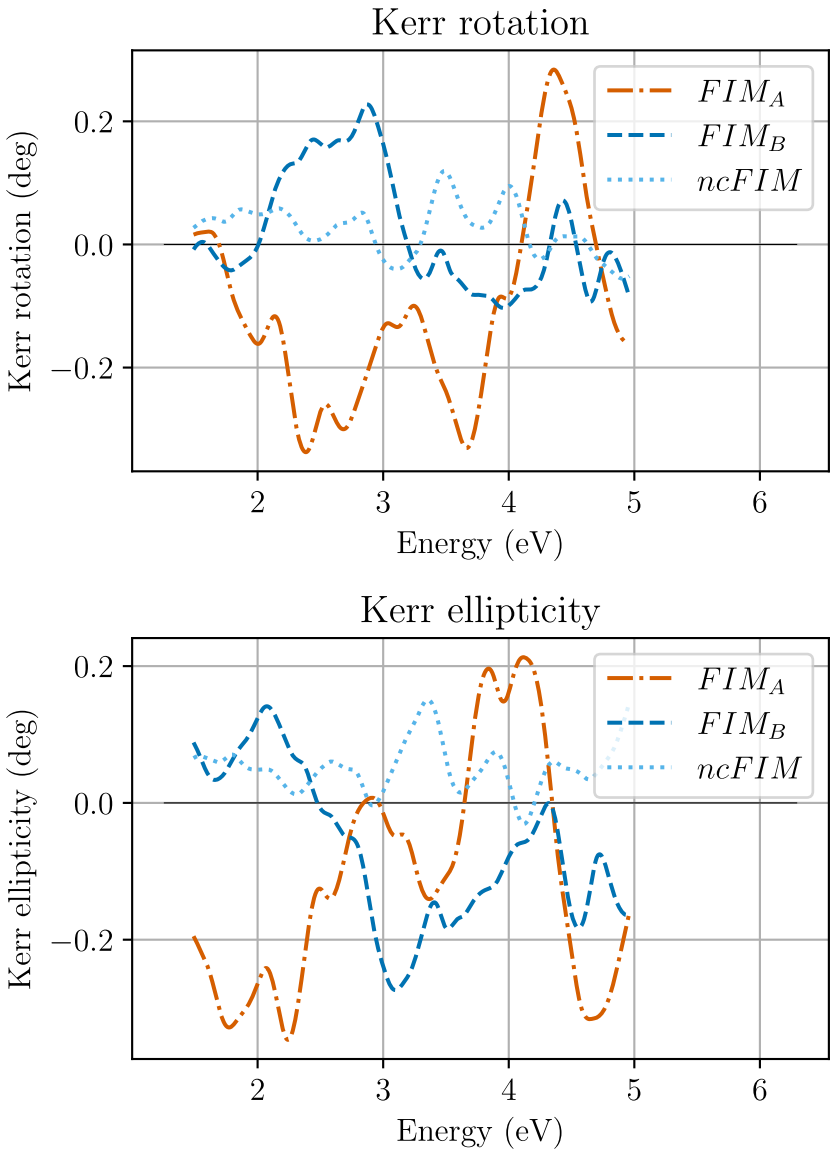

Figure 7.5: Theoretically simulated spectra for individual ferrimagnetic phases and sample structure analogous to sample 2.

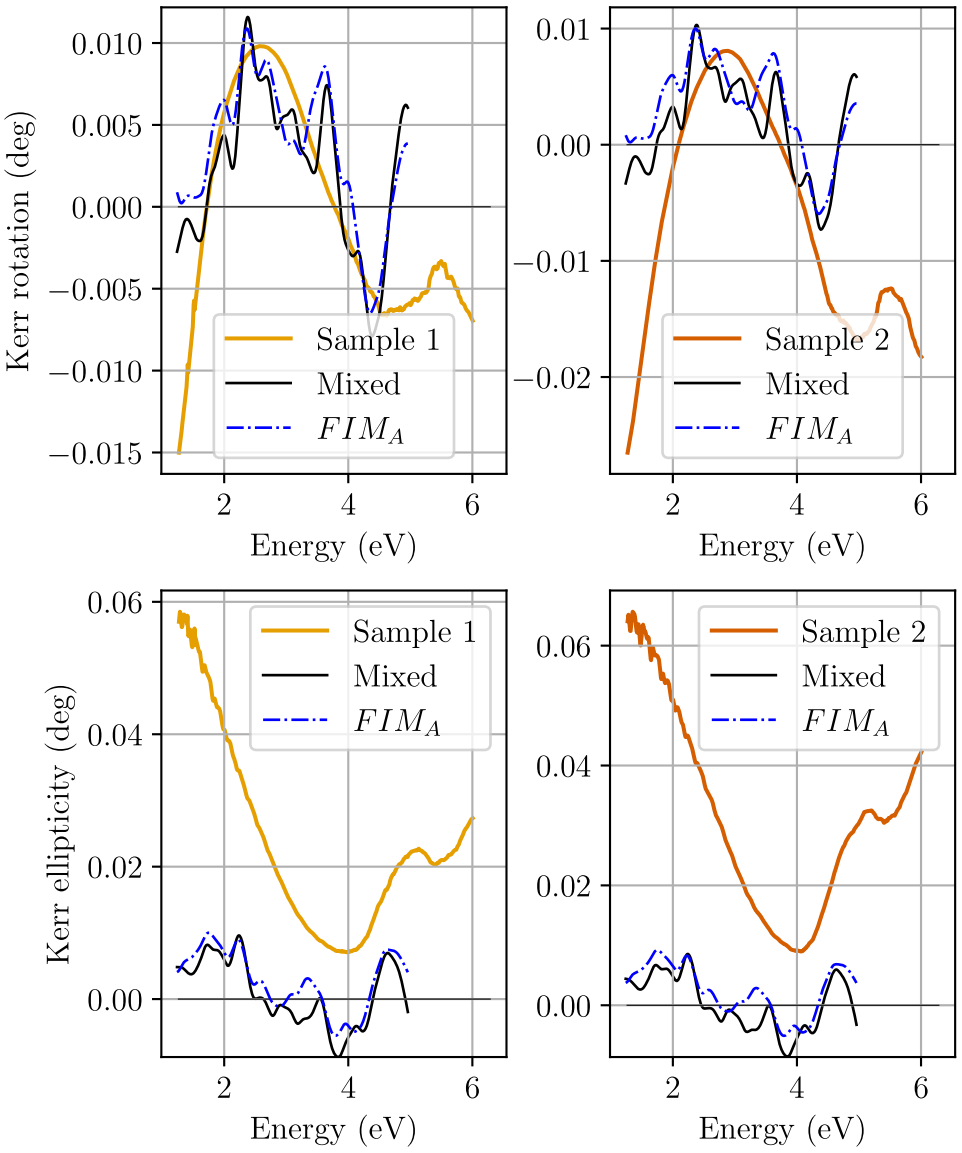

Figure 7.6: Comparison of experimentally measured and theoretically calculated MOKE spectra for pure FIM_A phase and a mix phases ncFIM and FIM_A with amplitudes adjusted to best match experimental data.

7.3.2 Kerr rotation dependence on temperature

Sample 4 was additionally measured using a modified magneto-optical setup coupled with a superconducting magnet (PPMS by Quantum Design), allowing for measurements at various temperatures and an external field of up to 9 T. The measurement setup was analogous to that in figure 5.2 with an additional window that the light had to pass through before and after reflecting from the sample placed in a cryostat. This introduces an unwanted Farraday rotation contribution from the window as it is not far enough to be fully shielded from the magnetic field. This Farraday rotation was determined by colleagues measuring other samples using the same setup and subtracted from the obtained results. The obtained Kerr rotation spectra for a range of temperatures from 20 to 300 K *with subtracted Farraday contribution from the window* can be found in figure 7.7. A zoomed in look at the measured spectra for temperatures between 20 and 80 K can be found in figure 7.8. Looking at figure 7.8, we can see that for the lowest temperatures, only noise is being measured. We would expect this noise to oscillate around 0, but instead the whole spectrum is shifted by about 5 mdeg. This is likely due to measurement error resulting for example from a non-perfect homing of the rotating analyzer in the measurement setup. However, we can see that the spectral characteristics clearly visible for high temperatures are still recognisable for lower temperatures all the way down to 40 K (see figures 7.7 and 7.8). This cannot be explained as a measurement error and since the spectra do not appear to change sign, we can estimate an upper bound on the compensation temperature of sample 4 of 40 K.

Comparing the spectra for $T = 300$ K from figure 7.7 and Kerr rotation spectra of sample 4 from 7.9, there does not appear to be a great agreement between the two. However, this is not too surprising, considering both spectra were measured at different field strengths (9 T vs 1 T). A ferrimagnetic material might respond differently to different external magnetic field strength as the individual sublattices may interact with the field differently.

Unfortunately there was not enough measurement time left to measure Kerr spectra temperature dependence for other samples.

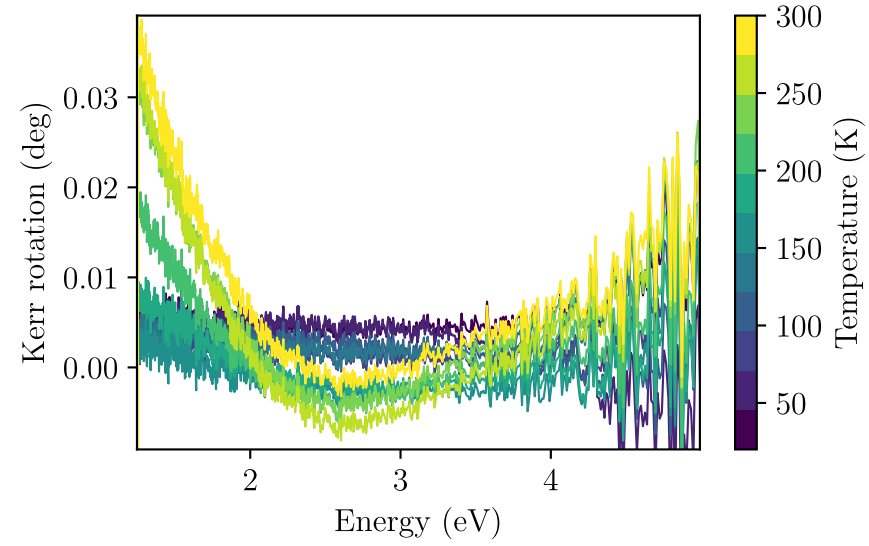

Figure 7.7: Spectral Kerr rotation measurements at temperatures ranging from 20 to 300 K with an external 9 T magnetic field.

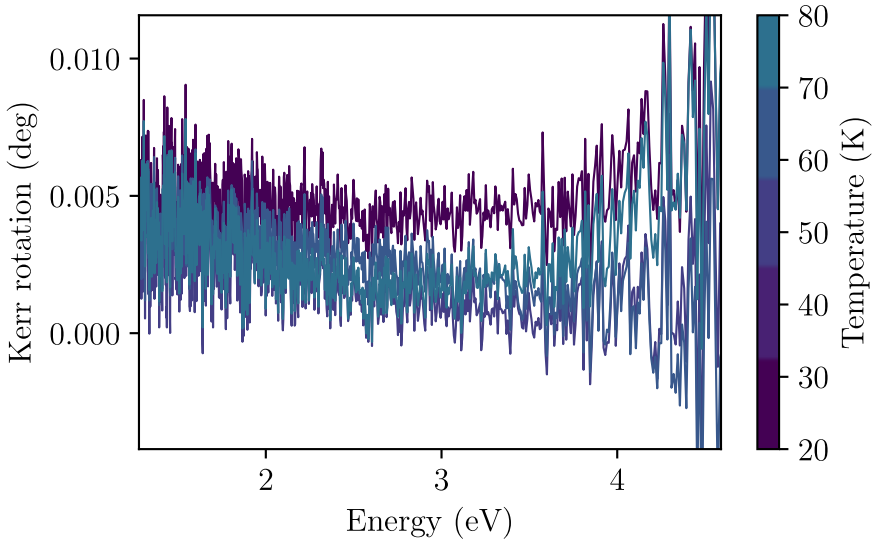

Figure 7.8: Spectral Kerr rotation measurements at temperatures ranging from 20 to 80K, zoomed in for easier discussion

7.3.3 MOKE hysteresis loops

For the two non-doped samples, MOKE spectra were measured for multiple external field strengths and hysteresis loops were constructed from the results. The measurements were performed at room temperature, with field strengths ranging from -1 T to 1 T. The obtained loops along with Kerr rotation spectra for all measured field values can be found in figure 7.9. The data in this figure has dynamically subtracted background (i.e the background subtraction was done independently for all pairs of data measured at field strengths of $\pm x$ T). To form the hysteresis loops, the one branch obtained from the mentioned background subtraction is duplicated and flipped to

complete the loop. From these measurements, we find the coercivity of our samples at room temperature to be $H_c = 0.51$ T in case of sample 1 and $H_c = 0.48$ T in case of sample 2. The measurements for sample 2 are less noisy because a better spectrometer was used. We can see, that the MOKE spectra do not cross zero at the same energy for all measured fields in the in UV region. This is likely a result of measurement error and parasitic Faraday rotation from the polarisers in the measurement setup. The magnitude of Faraday rotation if larger for higher energies, explaining, why the discrepancy in where the spectra measured for different fields cross zero is larger for higher energies. The measured hysteresis loop for sample 1 does not completely close, this is not physical and is again the result of measurement error.
Normalised hysteresis loops for multiple energies are plotted in figure 7.10, normalisation is necessary to get rid of the spectral dependence of Kerr rotation. Since the shape of the loops does not change with energy, we can conclude that the Kerr rotation in this part of the spectrum is dominated by only one sublattice of Mn_4N. This is also inline with the shape of the hysteresis loop resembling a ferromagnetic material with no apparent sign of mixing contributions from multiple sublattices as shown in 4.5.

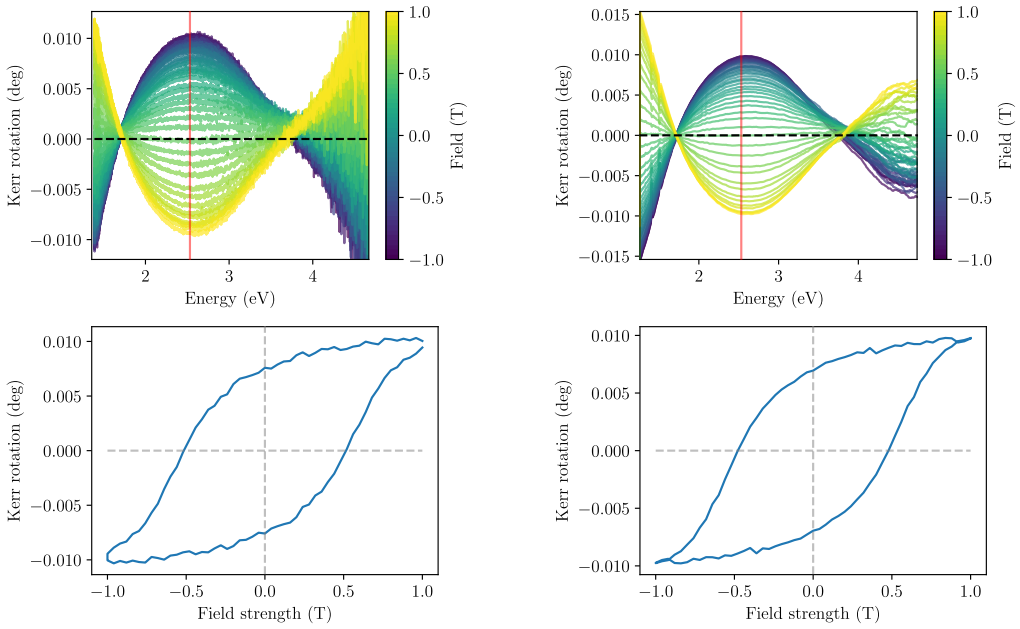

(a) Sample 1

(b) Sample 2

Figure 7.9: Kerr rotation spectra and hysteresis loops constructed from measurements at different field strengths. The hysteresis loops are plotted for 2.5 eV, as indicated by the red vertical lines.

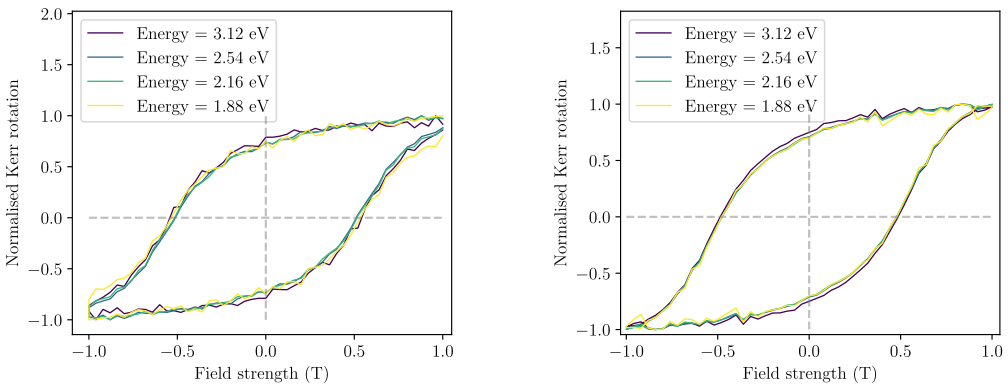

(a) Sample 1

(b) Sample 2

Figure 7.10: Normalised hysteresis loops plotted for multiple energies from 1.8 to 3.2 eV

Conclusion

Two samples with pure Mn_4N thin layer and three samples with Ga doped $Mn_{4-x}Ga_xN$ thin layer were analysed using spectroscopic ellipsometry and magneto-optical spectroscopy measurements.
From spectroscopic ellipsometry data, diagonal permittivity tensor element spectra were calculated. The obtained spectra of the imaginary part showed a spectral characteristic structure around 2.2 eV present in non-doped samples which disappeared in the case of the Ga doped samples, hinting at the presence of an electron transition of such energy linked to the corner Mn atoms which are being replaced by Ga atoms in the doping process. In the spectra of the imaginary part of the doped samples, a possible presence of a Lorentz oscillator at about 3 eV was discussed. This oscillator appears to shift to lower energies with higher Ga concentrations. Similar spectral characteristics shifting to lower energies with increased gallium concentrations were also observed in the spectra of the real part of the diagonal permittivity tensor elements.
From magneto-optical spectroscopy measurements, Kerr rotation and ellipticity spectra were calculated for all 5 measured samples. In the case of the two non-doped samples a significant peak between 2 and 4 eV was observed. For samples with Ga concentrations of x=0.11 and x=0.20, the obtained spectra were of far lower magnitude than for other samples. It was hypothesised that this might be caused by a relative proximity to the compensation temperature or the used external field not being strong enough to reach magnetic saturation. Between these two samples a sign reversal of the obtained Kerr rotation spectra was observed. The cause of this was determined to be the compensation temperature shifting from above room temperature for Ga concentration of x=0.11 to below room temperature for Ga concentration of 0.20. This result agrees nicely with [15].
Kerr rotation and ellipticity spectra of the two non-doped samples were compared with theoretical calculations based on material parameters taken from [2]. For the three proposed ferrimagmnetic phases, best agreement between experimental and theoretical spectra was observed for the FIM_A phase. It was also hypothesised, that a coexistence of the ncFIM and FIM_A phase might offer even better agreement between theory and experiment.
For the sample with Ga concentration of x=0.20, Kerr rotation spectra at temperatures ranging from 20 to 300 K were measured. From these measurements a high bound on the compensation temperature of this sample was determined at 40 K.
For the two non-doped samples, hysteresis loops were constructed from Kerr rotation data measured for multiple external magnetic field values. A coercivity values of $H_c = 0.51$ T in case of sample 1 and $H_c = 0.48$ T in case of sample 2 were determined. Furthermore, from the constant shape of the hysteresis loops for energies from 1.86 to 3.12 eV, it was determined that this part of the spectrum is dominated by only one sublattice of the ferrimagnetic Mn_4N.

As always, more measurements are needed. In the future we plan on finishing the temperature resolved Kerr rotation measurements for all available samples. This should allow us to better judge how the compensation temperature changes with gallium content and determine the usefullness of Ga doping in reaching near room temperature compensation temperature. Furthermore,we plan to measure MOKE hysteresis loops for the gallium doped samples at different temperatures to better understand how Ga doping changes the magnetic structure of Mn_4N.

Bibliography

[1] Takashi Suemasu, Laurent Vila, and Jean-Philippe Attané. "Present Status of Rare-earth Free Ferrimagnet Mn4N and Future Prospects of Mn4N-based Compensated Ferrimagnets". In: *Journal of the Physical Society of Japan* 90.8 (2021), p. 081010. DOI: 10.7566/JPSJ.90.081010.

[2] Jan Zemen. "Analysis of magneto-optical Kerr spectra of ferrimagnetic Mn_4N". In: *arXiv (Cornell University)* (2023). DOI: https://doi.org/10.48550/arxiv.2307.15246.

[3] Sambit Ghosh. "Manipulation of Domain Walls in Anti-perovskite Ferrimagnetic Nitrides". PhD thesis. July 2022.

[4] J. D. Jackson. *Classical electrodynamics, 3rd ed.* Wiley, 1999.

[5] Max Born et al. *Principles of Optics: Electromagnetic Theory of Propagation, Interference and Diffraction of Light*. Cambridge University Press, 1999.

[6] M. Nývlt. "Optical interactions in ultrathin magnetic film structures". PhD thesis. Charles University, 1996.

[7] W. Wettling. "Magneto-optics of ferrites". In: *Journal of Magnetism and Magnetic Materials* 3.1 (1976), pp. 147–160. ISSN: 0304-8853. DOI: https://doi.org/10.1016/0304-8853(76)90026-3.

[8] Stanislav Daniš. *Atomová Fyzika a elektronová Struktura Látek*. MatfyzPress, nakladatelství Matematicko-fyzikální fakulty Univerzity Karlovy, 2022.

[9] Roald K Wangsness. *Electromagnetic Fields*. en. 2nd ed. Nashville, TN: John Wiley & Sons, 1986.

[10] Robert M. White. *Quantum theory of magnetism:magnetic properties of materials*. Springer, 2007.

[11] Maria Losurdo et al. "Spectroscopic ellipsometry and polarimetry for materials and systems analysis at the nanometer scale: State-of-the-art, potential, and perspectives". In: *Journal of Nanoparticle Research* 11.7 (2009), 1521–1554. DOI: 10.1007/s11051-009-9662-6.

[12] W. J. Takei, G. Shirane, and B. C. Frazer. "Magnetic Structure of Mn_4N". In: *Phys. Rev.* 119 (1 1960), pp. 122–126. DOI: 10.1103/PhysRev.119.122.

[13] Daniel Fruchart et al. "The non-collinear component in the magnetic structure of Mn4N". In: *Journal of Physics F: Metal Physics* 9 (Jan. 2001), p. 2431. DOI: 10.1088/0305-4608/9/12/016.

[14] Taku Hirose et al. "Strong correlation between uniaxial magnetic anisotropic constant and in-plane tensile strain in Mn 4 N epitaxial films". In: *AIP Advances* 10 (Feb. 2020), p. 025117. DOI: 10.1063/1.5141818.

[15] Aoi Hatate et al. “X-ray magnetic circular dichroism of Mn4Ga N epitaxial thin films confirming ferrimagnetic-ferromagnetic phase transition by non-magnetic Ga doping”. In: *Journal of Magnetism and Magnetic Materials* (2024), 171973–171973. DOI: https://doi.org/10.1016/j.jmmm.2024.171973.

[16] M.D. Coye. personal communication.

[17] Tomohiro Yasuda, Kenta Amemiya, and Takashi Suemasu. “Growth of ultrathin Mn4N epitaxial films on SrTiO3(001) and their thickness-dependent magnetic structures”. In: *Applied physics letters* 123.12 (2023). DOI: https://doi.org/10.1063/5.0165783.

[18] Temuujin Bayaraa, Changsong Xu, and L Bellaiche. “Magnetization Compensation Temperature and Frustration-Induced Topological Defects in Ferrimagnetic Antiperovskite Mn4N”. In: *Physical review letters (Print)* 127.21 (2021). DOI: https://doi.org/10.1103/physrevlett.127.217204.

List of Figures